

$\lambda = 2$ mm spectroscopy observations toward the circumnuclear disk of NGC 1068

Jianjie Qiu¹, Jiangshui Zhang² *, Yong Zhang^{1,3} **, Lanwei Jia², Xindi Tang^{4,5,6}

¹ School of Physics and Astronomy, Sun Yat-sen University, Guangzhou 510275, PR China

² Center For Astrophysics, Guangzhou University, Guangzhou 510006, PR China

³ Laboratory for Space Research, University of Hong Kong, Hong Kong, PR China

⁴ Max-Planck-Institut für Radioastronomie, Auf dem Hügel 69, D-53121 Bonn, Germany

⁵ Xinjiang Astronomical Observatory, Chinese Academy of Sciences, 830011 Urumqi, PR China

⁶ Key Laboratory of Radio Astronomy, Chinese Academy of Sciences, PR China

January 24, 2020

ABSTRACT

Aims. We investigate the physical and chemical conditions of molecular gas in the circumnuclear disk (CND) region of NGC 1068.

Methods. We carried out a spectral line survey with the IRAM 30m telescope toward the center of NGC 1068 and mainly focused on the 2 mm band with a frequency coverage of 160.7–168.6 GHz and 176.5–184.3 GHz.

Results. Fifteen lines are detected in NGC 1068, eight of which are new detections for this galaxy. We derive the rotation temperatures and column densities of fourteen molecular species.

Conclusions. Based on the $[\text{HCO}^+(2-1)]/[\text{HOC}^+(2-1)]$ ratio, we obtain a high ionization degree in the CND of NGC 1068. It is found that HC_3N is concentrated in the east knot, while ^{13}CCH , CH_3CN , SO , HOC^+ , CS , CH_3CCH , and H_2CO are concentrated in the west knot. Compared to the star-forming galaxies M 82 and NGC 253, the chemistry of NGC 1068 might be less strongly affected by the UV radiation field, and its kinetic temperature might be lower.

Key words. ISM: molecules – galaxies: ISM – galaxies: individual: NGC 1068 – galaxies: nuclei – galaxies: active

1. Introduction

Molecular gas is the fuel of star formation. So far, more than 60 molecular species have been detected in external galaxies (McGuire 2018). The relative abundances of different species vary with its surrounding astrophysical environment (Omont 2007). The molecular rotational transition lines at millimeter wavelength are sensitive to and trace the physical and chemical properties of the interstellar medium. An unbiased line survey could detect molecular rotation transitions with different energy levels and/or different species and provide an unbiased view on the molecular environment. Previous observations at millimeter band have shown that the properties of molecular gas are different between starbursts (SB) and active galactic nuclei (AGN) in external galaxies (Kohnno et al. 2001; Krips et al. 2008; Izumi et al. 2013, 2016; Davis et al. 2013; Aladro et al. 2015; Nakajima et al. 2018; Li et al. 2019). The underlying causes of these variations, especially how the molecular composition might be affected by AGN, are still not fully clear.

NGC 1068 is one of the nearest (~ 14.4 Mpc, $1'' = 72$ pc, Bland-Hawthorn et al. 1997) and brightest ($L_{\text{IR}} = 3 \times 10^{11} L_{\odot}$) Seyfert II galaxies with a starburst. It consists of a starburst ring ($\sim 15''$ from the central AGN) and a central nuclear disk (CND) (Schinnerer et al. 2000). It was established that the physical conditions between the starburst ring and the CND are different (Viti et al. 2014). The molecular gas in the CND is denser and hotter than the gas in the starburst ring. Multi-gas-phase components exist in the CND region (Viti et al. 2014). The gas temperature

in the CND region is higher than 150 K, and the gas density is above 10^5 cm^{-3} (Viti et al. 2014). The CND region could be spatially resolved into an east and a west knot. These knots are dominated by a fast and a slow shock, respectively (Kelly et al. 2017). The mass of the central torus was estimated to be $2 \times 10^5 M_{\odot}$ (García-Burillo et al. 2014). With an AGN-driven outflow (García-Burillo et al. 2014) and a past inflow driven by a minor merger (Furuya & Taniguchi 2016), the torus shows a complex dynamical behavior (García-Burillo et al. 2016).

NGC 1068 is one of the best extragalactic targets for continuum and line observations in all wavelengths from X-rays to the radio domain (e.g., radio, Greenhill et al. 1996; millimeter, Schinnerer et al. 2000; infrared, Jaffe et al. 2004; optical, Antonucci & Miller 1985; UV, Antonucci et al. 1994; and X-ray, Kinkhabwala et al. 2002). These results show that the strong UV or X-ray field heavily influence the physical conditions, kinematics, and chemistry in the CND of NGC 1068 (Usero et al. 2004; Pérez-Beaupuits et al. 2009; García-Burillo et al. 2010; Nakajima et al. 2011, 2018; Aladro et al. 2011, 2015; Takano et al. 2014; Viti et al. 2014).

To better understand the chemistry in the CND of NGC 1068, we performed an observation of molecular lines at 3 mm bands (Qiu et al. 2018), and detected CH_3OCH_3 for the first time in external galaxies. As a supplement to the previous report, this paper presents observations of molecular lines at the 2 mm band toward NGC 1068. The organization of this paper is as follows: we present the observations and data reduction in Sect. 2, and the main results are provided in Sect. 3. We discuss the physical and chemical properties of molecules in Sect. 4, and give a brief summary in Sect. 5.

* e-mail: jszhang@gzhu.edu.cn

** e-mail: zhangyong5@mail.sysu.edu.cn

2. Observations and data reduction

The observations toward the center of NGC 1068 (RA: 02:42:40.70 DEC: -00:00:48.0 J2000) were carried out in January 2017 with the IRAM 30m single-dish telescope at Pico Veleta Observatory (Spain)¹. We used the Eight Mixer Receiver (EMIR) with dual polarization and the Fourier Transform Spectrometers (FTS) backend tuned. The frequency channel spacing was 195 KHz, and the instantaneous frequency coverage per sideband and polarization was 8 GHz. We used the standard wobbler-switching mode with a $\pm 110''$ offset and 1.5 second per phase. Each scan included eight subscans of 30 seconds. We checked pointing and focus every two hours.

The observations were performed using two tunings in the 2 mm window (160.7–168.6 GHz and 176.5–184.3 GHz) and in the 3 mm window (75.7–83.5 GHz and 91.4–99.2 GHz). The 3 mm spectra were obtained with a short integration time to supplement the line survey in the 2 mm window (Table 1). Figure 1 presents the full spectra. The molecular line temperature scale was converted from the antenna temperature T_A^* into the main beam temperature T_{mb} . The conversion relation between them is $T_{mb} = (F_{eff}/B_{eff}) \times T_A^*$, where F_{eff} and B_{eff} are the forward efficiency and main-beam efficiency of the telescope, respectively. The values assumed for F_{eff} and B_{eff} of each band are listed in Table 1. The main observation parameters, including band range, half-power bandwidth (HPBW), and spatial resolution, are also listed in Table 1.

The data reduction procedures are similar to those described in Qiu et al. (2018). Linear baseline subtraction and Gaussian profile fitting were made for all the detected lines. The data reduction was performed using the CLASS software of the GILDAS package². We identified each molecular transition by referring to the frequencies from the NIST database recommended rest frequencies for observed interstellar molecular microwave transitions³ and from the splatalogue database for astronomical spectroscopy⁴.

We performed a literature survey of previous observations made with single-dish telescopes toward NGC 1068. The lines detected by other research groups, together with those detected by us, are listed in Table 2. This table may serve as a reference source for future studies of this object. We assume a heliocentric systemic velocity $v_{sys} \sim 1137 \text{ km s}^{-1}$ (from NASA/IPAC Extragalactic Database (NED)⁵) for this source throughout.

3. Results

Overall, 15 lines belonging to 12 different molecular species are detected. Figure 2 shows the individual line profiles in velocity units, and Table 2 summarizes the parameters derived from Gaussian fitting with CLASS to the observed lines. The main results include the detection of the $J = 2 - 1$ transitions of ^{13}CCH , HCO^+ , HOC^+ , and HNC , and emission lines of CH_3OH ($J_{1,k-1} - J_{0,k}$)E, SO_2 ($5_{2,4} - 5_{1,5}$), and CH_3CN ($9_k - 8_k$). To our knowledge, these lines are detected for the first time in NGC 1068. In addition, we also detect the lines of CH_3CN ($5_k - 4_k$), N_2H^+ ($1 - 0$), CH_3OCH_3 ($3_{2,2} - 3_{1,3}$), CH_3OH ($2_k - 1_k$), CS ($2 - 1$), HC_3N ($18 - 17$), and HCN ($2 - 1$).

¹ This publication is based on data acquired with the IRAM 30-m telescope. IRAM is supported by INSU/CNRS (France), MPG (Germany), and IGN (Spain).

² CLASS <http://www.iram.fr/IRAMFR/GILDAS>

³ NIST <http://pml.nist.gov/cgi-bin/micro/table5/start.pl>

⁴ <http://www.cv.nrao.edu/php/splat/advanced.php>

⁵ <http://ned.ipac.caltech.edu>

CH_3CN ($5_k - 4_k$), HC_3N ($18 - 17$), and CH_3OCH_3 ($3_{2,2} - 3_{1,3}$), have been detected or tentatively detected in previous observations (Qiu et al. 2018). To enhance the signal-to-noise ratios (S/N), we combined the data of Qiu et al. (2018) for these three transitions. CH_3OCH_3 ($3_{2,2} - 3_{1,3}$) was only marginally detected toward NGC 1068 by Qiu et al. (2018). No stronger line is known in this wavelength. For this line, we also combined the spectral data of Aladro et al. (2013) and found that the S/N increases from 1.6 to 2.3, probably supporting the potential existence of CH_3OCH_3 in this galaxy. We checked the raw data of Qiu et al. (2018), and found that the CH_3CCH ($14_0 - 13_0$) line at 239 GHz is marginally detected, as shown in Fig. 2.

3.1. Line ratios

3.1.1. HCN/HCO⁺

Table 3 lists the velocity-integrated intensity ratio of the $J = 2 - 1$ transitions of five species, including ^{13}CCH , HCN , HCO^+ , HOC^+ , and HNC , detected in the CNB of NGC 1068. The flux ratio of HCN to HCO^+ can be used to distinguish galaxies powered by starburst and AGN (Kohno et al. 2001; Krips et al. 2008; Imanishi et al. 2009; Izumi et al. 2016; Aladro et al. 2018; Li et al. 2019). AGN galaxies usually exhibit higher $[\text{HCN}/\text{HCO}^+]$ ratios than starburst galaxies because high X-ray radiation in AGNs can enhance the abundance of HCN (Kohno et al. 2001; Privon et al. 2017). Our observations show that the flux ratio of HCN -to- HCO^+ ($J = 2 - 1$) is 1.82 ± 0.03 in the CNB of NGC 1068. This is consistent with previous interferometer observations at other J -transitions. For example, the flux ratio of HCN -to- HCO^+ is 1.6–2.0 at $J = 1 - 0$ (Viti et al. 2014), 1.6–3.3 at $J = 3 - 2$ (Imanishi et al. 2016), and 2.1–2.8 at $J = 4 - 3$ (Viti et al. 2014) in the nucleus of NGC 1068. Our single-dish and previous interferometer observational results confirm that the abundance of HCN is enhanced in the CNB of NGC 1068, which may be related to the outflow of AGN (García-Burillo et al. 2014).

3.1.2. HNC/HCN

HCN and its isomer HNC are tracers of dense gas, and commonly coexist in different environments (Gao & Solomon 2004; Aalto et al. 2012). Some galaxies exhibit a high HNC/HCN ratio, which may be caused by low temperature, high ion density, high optical depth, and/or IR pumping. Theoretical studies (Meijerink & Spaans 2005; Meijerink et al. 2007) suggest that the HNC/HCN ratio increases in X-ray dominated regions (XDRs) to a higher degree than that in photon-dominated regions (PDRs) and quiescent-cloud regions. Observations of three galaxies (Arp 220, NGC 4418, and Mrk 231), which have strong X-ray emission produced by embedded AGN, indicate a high HNC -to- HCN ($J = 3 - 2$) flux ratio of 1.9 ± 0.3 in Arp 220, 1.5 ± 0.2 in Mrk 231, and 2.3 ± 0.3 in NGC 4418 (Aalto et al. 2007). Our observations show that the integrated line ratio of HNC to HCN ($J = 2 - 1$) toward the CNB of NGC 1068 is 0.16 ± 0.03 . This is in agreement with $J = 3 - 2$ and $J = 4 - 3$ line ratios (0.15 ± 0.03 and 0.19 ± 0.02 , respectively; Pérez-Beaupuits et al. 2007, 2009). This means that we do not find enhanced HNC emission in the CNB of NGC 1068, and an XDR exists here. Because the HNC line is narrower than that of HCN , we exclude the IR pumping scenario: the IR pumping dominated scenario will show a broader line width of HNC than HCN , as described in Aalto et al. (2002). The ammonia (NH_3) observations show that some components of the molecular cloud have a higher temper-

ature of 140 ± 30 K in the CNB of NGC 1068 (Ao et al. 2011). A reasonable explanation of the lower HNC-to-HCN ratio is that the warmer molecular cloud leads to the HNC deficiency.

3.2. Line profile

The line profile can be taken as a diagnostic tool to investigate the properties of CNB molecular gas. Usero et al. (2004) found that all molecular line profiles in the CNB of NGC 1068 are distributed asymmetrically. They therefore suggested that the east and west knots of the CNB are chemically differentiated.

Previous interferometer observations of CO(1-0) showed that NGC 1068 has a circumnuclear molecular ring with diameter ranging from $\sim 20''$ to $40''$ (Schinnerer et al. 2000). The beam size of the IRAM 30m telescope at the 3 mm band is larger than the inner diameter of the two spiral arms of NGC 1068. In contrast, the beam sizes at the 2 mm and 1 mm bands are smaller than the inner diameter of the two spiral arms. The HPBW of HOC⁺(1-0) and (2-1), for instance, is about $27.5''$ at 89.5 GHz and $13.7''$ at 179.0 GHz, as shown in Fig. 3. High-resolution images show that the most prominent emission stems from the CNB (Takano et al. 2014; Viti et al. 2014). Therefore, the molecular lines lying within the 2 mm and 1 mm bands can preclude most of the contamination from the two spiral arms. Using a similar method as Usero et al. (2004), we divided each line into its blue and red velocity components (see Fig. 4), which dominantly arise from the east and west knots, respectively. The line profiles in Fig. 4 show that the local systemic velocity of these lines ranges from $v - v_{\text{sys}} = -200$ km s⁻¹ to 200 km s⁻¹. We defined the blue and red components as those lying within an interval of $-200 < v - v_{\text{sys}} < 0$ km s⁻¹ and $0 < v - v_{\text{sys}} < 200$ km s⁻¹, respectively. The velocity-integrated intensities of the two components are listed in Table 4. As shown in Fig. 4, there are noticeable differences between the line shapes of the CNB spectra. Some molecular lines, including HC₃N(18-17), SiO(5₅-4₄), SO₂(14_{3,11}-14_{2,12}), HNC(2-1), HCN(2-1), HCO⁺(2-1), HNCO(11-10), ¹³CCH(2-1), and CH₃CN(9-8), show a stronger blue component, while the others, including SO(5₅-4₄), HOC⁺(2-1), CS(5-4), CH₃CCH(14_k-13_k), and H₂CO(3_{1,2}-2_{1,1}), show a stronger red component.

Interferometer observations showed that the SiO(3-2) transition is dominantly distributed in the east knot and the HNCO(6-5) emission in the west knot (Kelly et al. 2017). Therefore, we hypothesize that the molecular species whose blue-to-red flux ratios are higher than that of SiO are mainly located in the east knot, while those with blue-to-red flux ratios lower than that of HNCO are mainly located in the west knot. Our single-dish observations of SiO(5₅-4₄) and HNCO(11-10) suggest a blue-to-red flux ratio ($R_{E/W}$) of 2.1 and 1.3, respectively. The blue-to-red flux ratio of HC₃N is higher than that of SiO, and thus is mainly located in the east knot. The blue-to-red flux ratios of the ¹³CCH(2-1), CH₃CN(9-8), SO(5₅-4₄), HOC⁺(2-1), CS(5-4), CH₃CCH(14_k-13_k), and H₂CO(3_{1,2}-2_{1,1}) transitions are lower than that of the HNCO(11-10) lines, and thus mainly arise from the west knot. The ¹³CCH(2-1), CH₃CN(9-8), and CH₃CCH(14-13) transitions include several multiple components, which may affect the determination of their blue-to-red flux ratios. However, as shown in Fig. 4, the strongest components have small frequency splits, suggesting that this effect can be neglected.

In Fig. 5 we compare the line profiles of HCN, HNC, HCO⁺, and HOC⁺ and those of the ¹³C isomers. We find that the ($J = 2-1$)-to-($J = 1-0$) flux ratios of HCN, HNC, and HCO⁺ are

higher for the blue components than those for the red components, while there is no significant difference for HOC⁺. Under the assumption of ¹²C/¹³C, Wang et al. (2014) suggested that the redshifted parts of HCN(1-0) and HCO⁺(1-0) have lower optical depths and more likely come from the spiral arms than from the nuclear region. Because the beam size of $J = 2-1$ is much smaller than that of $J = 1-0$, the different line profiles between the $J = 2-1$ and the $J = 1-0$ transitions may be attributed to the difference of their emission regions. The similar line profiles between the $J = 2-1$ lines of HCN and HCO⁺ and their isotopic lines (H¹³CN(1-0) and H¹³CO⁺(1-0)) suggest that they may come from the same location. The $J = 2-1$ and $J = 1-0$ transitions of HOC⁺ show similar profiles, suggesting that the molecule might be distributed in the CNB region.

HCN and HCO⁺ are tracers of dense gas. Their $J = 2-1$ transitions show similar line profiles and comparable velocities (see the lower panels of Fig. 5). Compared to the HCN(2-1) line, the HNC(2-1) line has a similar line center velocity, but a noticeably narrower line width. The HOC⁺(2-1)-to-HCO⁺(2-1) flux ratio in the blue component is higher than that in the red component. However, this is not the case for HNC and its isomer HCN. A possible explanation is that the $J = 2-1$ transitions of HCN, HNC, and HCO⁺ are associated with each other in the CNB of NGC 1068, while the HOC⁺(2-1) transition does not peak at the same position. This is consistent with the latest interferometer observation toward the center of the Seyfert II galaxy Mrk 273 (Aladro et al. 2018), which shows that the peak of the HOC⁺(3-2) emission is not at the same position as the dense gas of HCN and HCO⁺. Further observations with higher spatial resolution of HOC⁺ in the CNB of NGC 1068 are required to investigate the origin of this offset.

3.3. Rotation diagram

We applied the rotation diagram to derive excitation temperatures (T_{ex}) and column densities (N_{tot}) of the molecules we detected in our observations. With the assumption of local thermodynamic equilibrium (LTE), optically thin conditions, and negligible background temperature, we plot the populations of the upper levels (N_u) against the corresponding excitation energies (E_u) of the transitions (Fig. 6), using the equation

$$\ln \frac{N_u}{g_u} = \ln \frac{8\pi k \nu^2 \int T_s dv}{hc^3 A_{ul} g_u} = \ln \frac{N_{\text{tot}}}{Q(T_{\text{ex}})} - \frac{E_u}{kT_{\text{ex}}}, \quad (1)$$

where k is the Boltzmann constant, ν is the rest frequency of the transition, $Q(T_{\text{ex}})$ is the partition function, h is the Planck constant, c is the light speed, A_{ul} is the spontaneous emission coefficient, g_u is the total degeneracy of upper energy level, and E_u/k is the upper level energy. The values of $Q(T_{\text{ex}})$, A_{ul} , g_u , and E_u/k are taken from the Cologne Database for Molecular Spectroscopy (CDMS) catalog⁶ and the splatagogue astronomical spectroscopy database⁷. $\int T_s dv$ is the detected transition-integrated intensity. T_s is the source-averaged brightness temperature, corrected for beam dilution by $T_s = T_{\text{mb}}(\theta_b^2 + \theta_s^2)/\theta_s^2$, where θ_b is the antenna HPBW and θ_s is the source size. The antenna HPBW is estimated by $\text{HPBW}('') = 2460/\nu(\text{GHz})$. Following the assumption made by other researchers (e.g., Usero et al. 2004; Bayet et al. 2009; Krips et al. 2008; Aladro et al. 2013), we took a θ_s value of $4''$ that was obtained based on the interfer-

⁶ <https://cdms.astro.uni-koeln.de>

⁷ <http://www.cv.nrao.edu/php/splat/>

ometric observations of ^{12}CO , HCN, and ^{13}CO (Helfer & Blitz 1995; Schinnerer et al. 2000).

The rotation diagrams of the 14 molecular species detected in our observations are shown in Fig. 6. We combined previously published data for this plot. The derived values of T_{ex} and N_{tot} are listed in Table 5. Two components were considered to fit the rotation diagrams of 8 molecules, including CS, HCN, HCO^+ , HNC, SiO, CN, and CH_3OH . Alternatively, the nonlinear data distribution in the rotation diagrams can be caused by finite optical depths (Goldsmith, & Langer 1999). In this scenario, Eq. 1 is modified to

$$\ln \frac{N_u}{g_u} = \ln \frac{N_{\text{tot}}}{Q(T_{\text{ex}})} - \frac{E_u}{kT_{\text{ex}}} - \ln C_\tau, \quad (2)$$

where the optical depth correction factor $\ln C_\tau$ is expressed with $\ln C_\tau = \ln [\tau/(1 - e^{-\tau})]$. However, using the method developed by Goldsmith, & Langer (1999), we found that the C_τ value (< 0.005) is too low to fit the rotation diagrams.

The rotation temperatures of CS are consistent with the results derived by Aladro et al. (2013) within the errors, whereas the cold components of HC_3N and HCN have slightly higher rotation temperatures than the values obtained by Aladro et al. (2013). For HCO^+ , HNC, and SiO, the rotation temperatures derived by Aladro et al. (2013) lie between those of the cold and warm components. Because the $\text{SO}(5_6 - 4_5)$ and $\text{CH}_3\text{CN}(12 - 11)$ transitions are strongly blended with the wings of the strong $^{13}\text{CO}(2 - 1)$ and $\text{C}^{18}\text{O}(2 - 1)$ transitions, their fluxes represent upper limits; see Qiu et al. (2018). These two transitions were excluded in fitting the rotational diagrams. The rotation temperature of SO is lower than that derived by Aladro et al. (2013) ($\sim 22.8 \pm 18.6$ K). Because they deviate from the fitting lines, we did not use the transitions of $\text{SO}(5_4 - 4_4)$, $\text{HNCO}(6_{1,6} - 5_{1,5})$, $(5_{1,4} - 4_{1,3})$, and $(5_{1,5} - 4_{1,4})$ in the rotation diagrams.

3.4. Molecular transitions detected with different single-dish telescopes

Some of the molecular transitions have been detected by single-dish telescopes with different beam sizes. NGC 1068 consists of a starburst ring and a CND. As shown in Fig. 1 of Takano et al. (2019), the beam of the IRAM 30m telescope covers the CND and starburst ring at the 3 mm band, while the beam of the NRO 45m telescope only covers the CND. In the 1 and 2 mm windows, the JCMT beam covers the CND and starburst ring, while the beam of the IRAM 30m telescope only covers the CND. By comparing the main-beam temperatures of a certain transition detected by different telescopes, we could roughly estimate the size of the regions from which this molecule arises. This approach has been used by Takano et al. (2019) to study the molecular emission regions in NGC 1068 and NGC 253. The authors concluded that the distributions of molecules between these two galaxies are significantly different. Combining these results with the data in the literature, we calculated the ratios between the observed intensities by different telescopes for 28 transitions (see Table 6).

When the beams cover the same emission regions (i.e., the CND), the intensities measured by the telescope with the wider beam should be lower because of the beam-dilution effect, and thus the ratios shown in Fig. 7 should be higher than unity. However, we find that the ratios for $^{13}\text{CO}(1 - 0)$, $\text{CH}_3\text{OH}(2_k - 1_k)$, HNC(1 - 0), $^{13}\text{CO}(2 - 1)$, HCN(3 - 2), $\text{C}^{18}\text{O}(1 - 0)$, CO(1 - 0), SiO(2 - 1), $\text{HCO}^+(1 - 0)$, and CS(2 - 1) are lower than unity, suggesting that the surrounding starburst ring may significantly contribute to these transitions. Theoretically, the line

intensity ratio decreases with increasing percentage of the line emission from the starburst ring. The lines with intensity ratios much higher than unity may be mainly distributed in the CND. This is supported by interferometer observations. For instance, $^{13}\text{CN}(1_{1/2} - 0_{1/2})$, $\text{HC}_3\text{N}(11 - 10)$, $\text{HNCO}(5_{0,5} - 4_{0,4})$, and $\text{CH}_3\text{CN}(6_k - 5_k)$ have high intensity ratios. The ALMA observations of Takano et al. (2014) showed that they are concentrated in the CND. Significant contributions from the ring have been revealed by ALMA for the $^{13}\text{CO}(1 - 0)$ emission, which has a low intensity ratio (Fig. 7). The intensity ratio of the CS(2 - 1) line is close to unity, again in agreement with the ALMA observations that reveal low contributions from the ring.

Assuming that the telescopes with different beam sizes detect the same molecular regions, we can derive the source size by the expression

$$\theta_s = \sqrt{\frac{I_2 \times \theta_{b2}^2 - I_1 \times \theta_{b1}^2}{I_1 - I_2}}, \quad (3)$$

where I_1 and I_2 are the integrated intensities detected with two different telescopes, and θ_{b1} and θ_{b2} are the beam sizes of the corresponding telescopes. As shown in Fig. 7 and Table 6, the estimated source sizes are generally larger than $4''$. However, these calculations sensitively depend on the intensity ratio and on the assumption of a Gaussian brightness distribution. Low pollution from outside of the CND may substantially increase the estimated θ_s value. Nevertheless, the assumption of $\theta_s = 4''$ does not significantly affect the results we obtain from the rotation diagrams. With θ_s increasing by a factor of two, the derived column densities would decrease by about 10%, while the rotation temperatures would be maintained at the same level.

4. Discussion

4.1. HOC^+ in XDR

Based on the observations of HCN and its isomer HNC in interstellar clouds, Herbst et al. (1976) hypothesized that if HNC is present in interstellar clouds, then HOC^+ , the energetically disfavored HCO^+ isomer, is also present. Subsequently, the $\text{HOC}^+(1 - 0)$ transition was detected toward Sgr B2 by Woods et al. (1983) and Ziurys & Apponi (1995), based on the experimental work of Gudeman & Woods (1982). So far, HOC^+ has been detected in diverse environments in our Galaxy and external galaxies, including diffuse clouds (Liszt et al. 2004), an ultracompact HII region (Rizzo et al. 2003), PDRs (Apponi et al. 1999; Fuente et al. 2003), dense molecular clouds (Apponi & Ziurys 1997), starburst galaxies (Fuente et al. 2005; Martín et al. 2009a; Aladro et al. 2015), and Seyfert galaxies (Usero et al. 2004; Aalto et al. 2015; Aladro et al. 2018). These observations suggest that HOC^+ is widespread in the interstellar medium, with the $[\text{HOC}^+]$ -to- $[\text{HCO}^+]$ ratio varying from tens to some thousand. The formation routes of HOC^+ and its isomer HCO^+ were described by Aladro et al. (2018) and references therein. Interferometer observations toward Mrk 273, a nearby Seyfert II galaxy, show a global $\text{HCO}^+/\text{HOC}^+(J = 3 - 2)$ brightness temperature ratio of 9 ± 4 and nuclear ratio of 5 ± 3 (Aladro et al. 2018). HOC^+ was tentatively detected toward the nucleus of Mrk 231, which hosts a powerful AGN, with the $\text{HCO}^+/\text{HOC}^+(J = 3 - 2)$ brightness temperature ratio ranging from 10 to 20 (Aalto et al. 2015). These values are generally lower than those in other sources, suggesting that the AGN might be associated with enhanced HOC^+ .

We detect the $J = 2 - 1$ transitions of both HCO^+ and HOC^+ in the CNB of NGC 1068, allowing us to further investigate the association between AGN and the HOC^+ enhancement. Figure 3 presents the CO(1-0) map overlaid by beam sizes of the IRAM 30m telescope at the HOC^+ (1-0) and (2-1) lines. The HPBW at the HOC^+ (1-0) line is larger than the inner diameter of the starburst ring, while that of the HOC^+ (2-1) line is smaller. This means that the HOC^+ (2-1) emission dominantly arises from the CNB region and not from the two spirals that are dominated by star formation. The situations are the same with the HCO^+ (1-0) and (2-1) transitions. Figure 8 shows the transitions of $J = 1 - 0$ and $J = 2 - 1$ of HCO^+ and HOC^+ , as well as the HCO^+ -to- HOC^+ temperature ratio profiles. The HCO^+ -to- HOC^+ temperature ratio of each velocity channel ranges from 32 to 109 and from 7 to 27 for the $J = 1 - 0$ and $J = 2 - 1$ transitions, respectively. These low values are consistent with the results of Usero et al. (2004), who suggested that the high electron density in the XDR may lead to a low $[\text{HCO}^+]/[\text{HOC}^+]$ ratio. HCO^+ and HOC^+ in the XDR are produced through three chemical paths ($\text{CO} + \text{H}_3^+$, $\text{CO}^+ + \text{H}_2$, and $\text{H}_2\text{O} + \text{C}^+$) (Maloney et al. 1996; Sternberg & Dalgarno 1995). The HCO^+ and HOC^+ fractions formed in these paths were illustrated by Usero et al. (2004) (see their Fig. 8). Our detections suggest that the integrated intensity ratio of $\text{HCO}^+/\text{HOC}^+$ ($J = 2 - 1$) is 15.8 ± 3.0 , which indicates an electron abundance with $n(e^-)/n(\text{H}_2) = 10^{-4.6}$ according to the XDR model of Usero et al. (2004). The $\text{CO} + \text{H}_3^+$ and $\text{H}_2\text{O} + \text{C}^+$ routes dominate the production of HCO^+ and HOC^+ . The high ionization degree suggests strong X/UV irradiation powered by AGN.

As shown in Fig. 8, the profiles of the HOC^+ (1-0) and (2-1) lines are noticeably asymmetrical with respect to v_{sys} . The asymmetry can be quantified by the ratio between the integrated fluxes in the blue and red parts relative to the central frequency. In Table 4 we compare the blue-to-red flux ratio of HOC^+ line with those of other lines. We find that the ratio for HOC^+ (2-1) is 0.93, differing from those of HNC (2-1) (~ 1.70), HCN (2-1) (~ 1.47), and HCO^+ (2-1) (~ 1.38). This might suggest that HOC^+ has a different distribution than HNC , HCN , and HCO^+ . We note that the spatial resolved observations toward Mrk 273 also showed different peak positions of the HOC^+ , HNC , HCN , and HCO^+ lines (Aladro et al. 2018). Therefore, we hypothesize that the formation of HOC^+ is more sensitive to the environments of the XDR than the formation of other molecules. Future interferometer observations of HOC^+ in NGC 1068 would allow a firmer conclusion.

4.2. Comparison of the molecules in NGC 1068, M82, and NGC 253

To investigate the roles of AGN and starburst on molecular chemistry, we compared the molecular lines detected in NGC 1068 and in the two nearby typical starburst galaxies M82 and NGC 253. M82 is a prototype starburst galaxy with a high star formation rate ($\sim 9 M_{\odot} \text{ yr}^{-1}$, Strickland et al. 2004) at a distance of ~ 3.6 Mpc (Freedman et al. 1994). NGC 253 is an almost edge-on barred spiral galaxy with an active nuclear starburst ($\sim 3.6 M_{\odot} \text{ yr}^{-1}$, Strickland et al. 2004 at a distance of ~ 3 Mpc (Mouhcine et al. 2005). The star formation in M82 and NGC 253 is in the middle and later stages, respectively. The unbiased line surveys of NGC 253 (Martín et al. 2006) and M82 (Aladro et al. 2011) at the millimeter band have revealed that the two galaxies have clearly different chemical characteristics. In Figs. 9 and 10 we compare the rotation temperatures, column densities, and fraction abundances of nine detected molecular

species in three galaxies, including SiO, CH_3CN , HC_3N , SO_2 , SO, HNC, CS, CH_3OH , and CH_3CCH . The molecular rotation temperatures in NGC 1068 are generally lower than the temperatures in M82 and NGC 253. The only exception is the warm component of CS. CS is a dense-gas tracer. Its high temperature probably suggests that the IR-photon heating, resulting from dust emission, is effective inside of the CS molecular cloud. Therefore, we conclude that the interior of the dense molecular cloud in the CNB of NGC 1068 is more severely obscured by dust than the interiors in M82 and NGC 253. The heavy dust obscuration significantly shield molecules from a strong UV/X-ray radiation field, leading to the enhancement of complex molecules such as CH_3OCH_3 .

As shown in the upper panel of Fig. 10, the column densities of molecular species in NGC 1068 are higher than those in M82 and NGC 253 by one to two orders of magnitude, suggesting that NGC 1068 is a rich reservoir of molecules. The fraction abundance of SiO in NGC 1068 is clearly larger than those in M82 and NGC 253 (see the lower panel of Fig. 10). This is consistent with the interferometer observations of SiO(3-2), which suggest that SiO is enhanced by a fast shock in the east knot of CNB of NGC 1068 (Kelly et al. 2017).

The $[\text{c-C}_3\text{H}_2]/[\text{HC}_3\text{N}]$ ratio can be used to trace the evolutionary stages of the star formation (Fuente et al. 2005). Taking the column density of $\text{c-C}_3\text{H}_2$ obtained by Nakajima et al. (2011), we derive $[\text{c-C}_3\text{H}_2]/[\text{HC}_3\text{N}] = 0.07$ for NGC 1068, which is lower than that in M82 (~ 2) and NGC 253 (~ 0.2). This suggests that the UV radiation field plays a less important role in the chemistry of NGC 1068 than that in M82 and NGC 253, where HC_3N is significantly dissociated and the cyclic molecule $\text{c-C}_3\text{H}_2$ is more resistant to UV photons.

CH_3CCH has a small dipole moment (0.75 Debye), and thus its rotation temperature should be close to the kinetic temperature of the molecular cloud. It follows that the kinetic temperature in NGC 1068 is the lowest of the three galaxies. Through a large velocity gradient (LVG) analysis, Krips et al. (2008) obtained that the kinetic temperature of M82 is 60–100 K. However, there are two solutions for the kinetic temperature of NGC 1068 (20 K and 60–240 K). The lower solution is close to the rotational temperature of CH_3CCH (28.0 ± 3.4 K).

The profile of the $\text{SO}(5_5 - 4_4)$ line suggests that SO is concentrated in the west knot of CNB. Based on models of ice evaporation process, Viti et al. (2004) suggested that SO is much more abundant than SO_2 at the beginning of the high-mass star formation, while the reverse is the case in the hot core. The ALMA 1.1 mm continuum emission showed that an ongoing star formation signature existed in the southwestern direction of the AGN with a distance of about 2 arcsecond (Imanishi et al. 2016). Therefore, it is likely that SO is enhanced by star formation in the west knot of the CNB in NGC 1068. In contrast, the blue-to-red flux ratio of the $\text{SO}_2(5_5 - 4_4)$ line (~ 2.05) is close to that of the $\text{SiO}(5_5 - 4_4)$ line (~ 2.08). Therefore, we infer that SO_2 is more concentrated in the east knot. Figure 10 shows that SO_2 is more abundant than SO in both NGC 1068 and NGC 253. This can be explained by the chemical model of Viti et al. (2004), according to which SO_2 is more abundant than SO within the post-shock gas. Previous observations have shown that the nuclear molecular clouds of NGC 253 are dominated by large-scale low-velocity shocks (Martín et al. 2006) and that the east and west knot of NGC 1068 are dominated by a fast and a slow shock, respectively (Kelly et al. 2017). Figure 10 also shows that the abundance ratio of SO/SO_2 in NGC 1068 is lower than that in NGC 253. SO_2 can be photodissociated by interstellar UV radiation to form SO (Willacy & Millar 1997). The lower $[\text{SO}]/[\text{SO}_2]$

ratio in NGC 1068 is consistent with our conclusion that the UV radiation field plays a less important role in the chemistry of NGC 1068 than in that of NGC 253.

5. Summary

We reported an observation toward the nuclear region of NGC 1068 at the 2 mm bands. The chemical properties of the CND in NGC 1068 were investigated. Our main conclusions are as follows.

1. Fifteen emission lines toward the center of NGC 1068 are detected, eight of which are the first detection in this source. Based on the line profile diagnosis of molecular gas in CDN, we infer that HC_3N and SO_2 are mainly concentrated in the east knot of the CND, while ^{13}CCH , CH_3CN , SO , HOC^+ , CS , CH_3CCH , and H_2CO are in the west knot of the CND.

2. The CND of NGC 1068 is highly ionized with an ionization degree of $X(e^-) \sim 10^{-4.6}$. The high ionization degree is consistent with the spacial distribution of HOC^+ , which is enhanced in XDR and is mainly distributed in the CND of NGC 1068 and not in the surrounding starburst ring.

3. Based on the rotation-diagram, we derived the column densities and rotation temperatures of 14 molecular species in NGC 1068. With these results, we find that the physical conditions and chemical environments in NGC 1068 may significantly differ from those in NGC 253 and M 82: the UV radiation filed in NGC 1068 is lower than that in M 82 and NGC 253, and NGC 1068 has the lowest kinetic temperature.

It is clear that the CND of NGC 1068 has complex chemical environments. This paper demonstrates that the data obtained by single-dish telescopes can provide significant supplements to interferometer observations in investigating the physical and chemical environments of galaxies.

Acknowledgements. We thank the anonymous referee for the useful comments that improved the manuscript. This work was supported by the Natural Science Foundation of China (NSFC) awarded to YZ (No. 11973099) and the China Postdoctoral Science Foundation funded project (No. 2019M653144) awarded to JJQ. JSZ thanks the support of NSFC (No. 11590782). LWJ appreciates support by the Guangzhou Education Bureau (No. 1201410593). JJQ wishes to thank Dr. Jun-Zhi Wang for his useful suggestions and Mr. Deng-Rong Lu for his help with the data reduction. XDT acknowledges support by the Heaven Lake Hundred-Talent Program of Xinjiang Uygur Autonomous Region of China. We wish to express my gratitude to the staff at the IRAM 30m telescope for their kind help and support during our observations.

References

Aalto, S., Polatidis, A. G., Hüttemeister, S., & Curran, S. J. 2002, *A&A*, 381, 783
Aalto, S., Spaans, M., Wiedner, M. C., & Hüttemeister, S. 2007, *A&A*, 464, 193
Aalto, S., García-Burillo, S., Müller, S., et al. 2012, *A&A*, 537, A44
Aalto, S., Martín, S., Costagliola, F., et al. 2015, *A&A*, 584, A42
Aladro, R., Martín, S., Martín-Pintado, J., et al. 2011, *A&A*, 535, AA84
Aladro, R., Viti, S., Bayet, E., et al. 2013, *A&A*, 549, AA39
Aladro, R., Martín, S., Riquelme, D., et al. 2015, *A&A*, 579, A101
Aladro, R., König, S., Aalto, S., et al. 2018, *A&A*, 617, A20
Antonucci, R. R. J., & Miller, J. S. 1985, *ApJ*, 297, 621
Antonucci, R., Hurt, T., & Miller, J. 1994, *ApJ*, 430, 210
Ao, Y., Henkel, C., Braatz, J. A., et al. 2011, *A&A*, 529, A154
Apponi, A. J., Pesch, T. C., & Ziurys, L. M. 1999, *ApJ*, 519, L89
Apponi, A. J., & Ziurys, L. M. 1997, *ApJ*, 481, 800
Bayet, E., Aladro, R., Martín, S., Viti, S., & Martín-Pintado, J. 2009, *ApJ*, 707, 126
Bland-Hawthorn, J., Gallimore, J. F., Tacconi, L. J., et al. 1997, *Ap&SS*, 248, 9
Costagliola, F., Aalto, S., Rodríguez, M. I., et al. 2011, *A&A*, 528, A30
Davis, T. A., Heiderman, A., Evans, N. J., & Iono, D. 2013, *MNRAS*, 436, 570
Freedman, W. L., Hughes, S. M., Madore, B. F., et al. 1994, *ApJ*, 427, 628
Fuente, A., García-Burillo, S., Gerin, M., et al. 2005, *ApJ*, 619, L155

Fuente, A., Rodríguez-Franco, A., García-Burillo, S., Martín-Pintado, J., & Black, J. H. 2003, *A&A*, 406, 899
Furuya, R. S., & Taniguchi, Y. 2016, *PASJ*, 68, 103
Gao, Y., & Solomon, P. M. 2004, *ApJS*, 152, 63
García-Burillo, S., Combes, F., Usero, A., et al. 2014, *A&A*, 567, AA125
García-Burillo, S., Combes, F., Ramos Almeida, C., et al. 2016, *ApJ*, 823, L12
García-Burillo, S., Usero, A., Fuente, A., et al. 2010, *A&A*, 519, AA2
Goldsmith, P. F., & Langer, W. D. 1999, *ApJ*, 517, 209
Greenhill, L. J., Gwinn, C. R., Antonucci, R., & Barvainis, R. 1996, *ApJ*, 472, L21
Gudeman, C. S., & Woods, R. C. 1982, *Physical Review Letters*, 48, 1344
Herbst, E., Norbeck, J. M., Certain, P. R., & Klemperer, W. 1976, *ApJ*, 207, 1110
Helfer, T. T., & Blitz, L. 1995, *ApJ*, 450, 90
Huettemeister, S., Henkel, C., Mauersberger, R., et al. 1995, *A&A*, 295, 571
Imanishi, M., Nakanishi, K., Tamura, Y., & Peng, C.-H. 2009, *AJ*, 137, 3581
Imanishi, M., Nakanishi, K., & Izumi, T. 2016, *ApJ*, 822, L10
Izumi, T., Kohno, K., Aalto, S., et al. 2016, *ApJ*, 818, 42
Izumi, T., Kohno, K., Martín, S., et al. 2013, *PASJ*, 65, 100
Israel, F. P. 2009, *A&A*, 493, 525
Jaffe, W., Meisenheimer, K., Röttgering, H. J. A., et al. 2004, *Nature*, 429, 47
Jiang, X.-J., Wang, J.-Z., Gao, Y., et al. 2017, *A&A*, 600, A15
Kamenetzky, J., Glenn, J., Maloney, P. R., et al. 2011, *ApJ*, 731, 83
Kelly, G., Viti, S., García-Burillo, S., et al. 2017, *A&A*, 597, A11
Kinkhabwala, A., Sako, M., Behar, E., et al. 2002, *ApJ*, 575, 732
Kohno, K., Matsushita, S., Vila-Vilaró, B., et al. 2001, *The Central Kiloparsec of Starbursts and AGN: The La Palma Connection*, 249, 672
Krips, M., Neri, R., García-Burillo, S., et al. 2008, *ApJ*, 677, 262
Li, F., Wang, J., Kong, M., & Li, S. 2019, *MNRAS*, 482, 4763
Liszt, H., Lucas, R., & Black, J. H. 2004, *A&A*, 428, 117
Maloney, P. R., Hollenbach, D. J., & Tielens, A. G. G. M. 1996, *ApJ*, 466, 561
Martín, S., Mauersberger, R., Martín-Pintado, J., Henkel, C., & García-Burillo, S. 2006, *ApJS*, 164, 450
Martín, S., Martín-Pintado, J., & Viti, S. 2009a, *ApJ*, 706, 1323
Martín, S., Martín-Pintado, J., & Mauersberger, R. 2009b, *ApJ*, 694, 610
Mauersberger, R., Henkel, C., Wilson, T. L., & Harju, J. 1989, *A&A*, 226, L5
McGuire, B. A. 2018, *ApJS*, 239, 17
Meijerink, R., & Spaans, M. 2005, *A&A*, 436, 397
Meijerink, R., Spaans, M., & Israel, F. P. 2007, *A&A*, 461, 793
Mouhcine, M., Ferguson, H. C., Rich, R. M., Brown, T. M., & Smith, T. E. 2005, *ApJ*, 633, 810
Nakajima, T., Takano, S., Kohno, K., & Inoue, H. 2011, *ApJ*, 728, LL38
Nakajima, T., Takano, S., Kohno, K., Harada, N., & Herbst, E. 2018, *PASJ*, 70, 7
Omont, A. 2007, *Reports on Progress in Physics*, 70, 1099
Paglione, T. A. D., Jackson, J. M., & Ishizuki, S. 1997, *ApJ*, 484, 656
Pérez-Beaupuits, J. P., Aalto, S., & Gerebro, H. 2007, *A&A*, 476, 177
Pérez-Beaupuits, J. P., Spaans, M., van der Tak, F. F. S., et al. 2009, *A&A*, 503, 459
Privon, G. C., Aalto, S., Falstad, N., et al. 2017, *ApJ*, 835, 213
Qiu, J., Shi, Y., Wang, J., Zhang, Z.-Y., & Zhou, L. 2017, *ApJ*, 846, 68
Rizzo, J. R., Fuente, A., Rodríguez-Franco, A., & García-Burillo, S. 2003, *ApJ*, 597, L153
Schinnerer, E., Eckart, A., Tacconi, L. J., Genzel, R., & Downes, D. 2000, *ApJ*, 533, 850
Sternberg, A., & Dalgarno, A. 1995, *ApJS*, 99, 565
Strickland, D. K., Heckman, T. M., Colbert, E. J. M., Hoopes, C. G., & Weaver, K. A. 2004, *ApJ*, 606, 829
Takano, S., Nakajima, T., Kohno, K., et al. 2014, *PASJ*, 66, 75
Takano, S., Nakajima, T., & Kohno, K. 2019, *PASJ*, 65
Tan, Q.-H., Gao, Y., Zhang, Z.-Y., et al. 2018, *ApJ*, 860, 165
Usero, A., García-Burillo, S., Fuente, A., Martín-Pintado, J., & Rodríguez-Fernández, N. J. 2004, *A&A*, 419, 897
Viti, S., Collings, M. P., Dever, J. W., McCoustra, M. R. S., & Williams, D. A. 2004, *MNRAS*, 354, 1141
Viti, S., García-Burillo, S., Fuente, A., et al. 2014, *A&A*, 570, A28
Wang, J., Zhang, Z.-Y., Qiu, J., et al. 2014b, *ApJ*, 796, 57
Willacy, K., & Millar, T. J. 1997, *A&A*, 324, 237
Woods, R. C., Gudeman, C. S., Dickman, R. L., et al. 1983, *ApJ*, 270, 583
Ziurys, L. M., & Apponi, A. J. 1995, *ApJ*, 455, L73

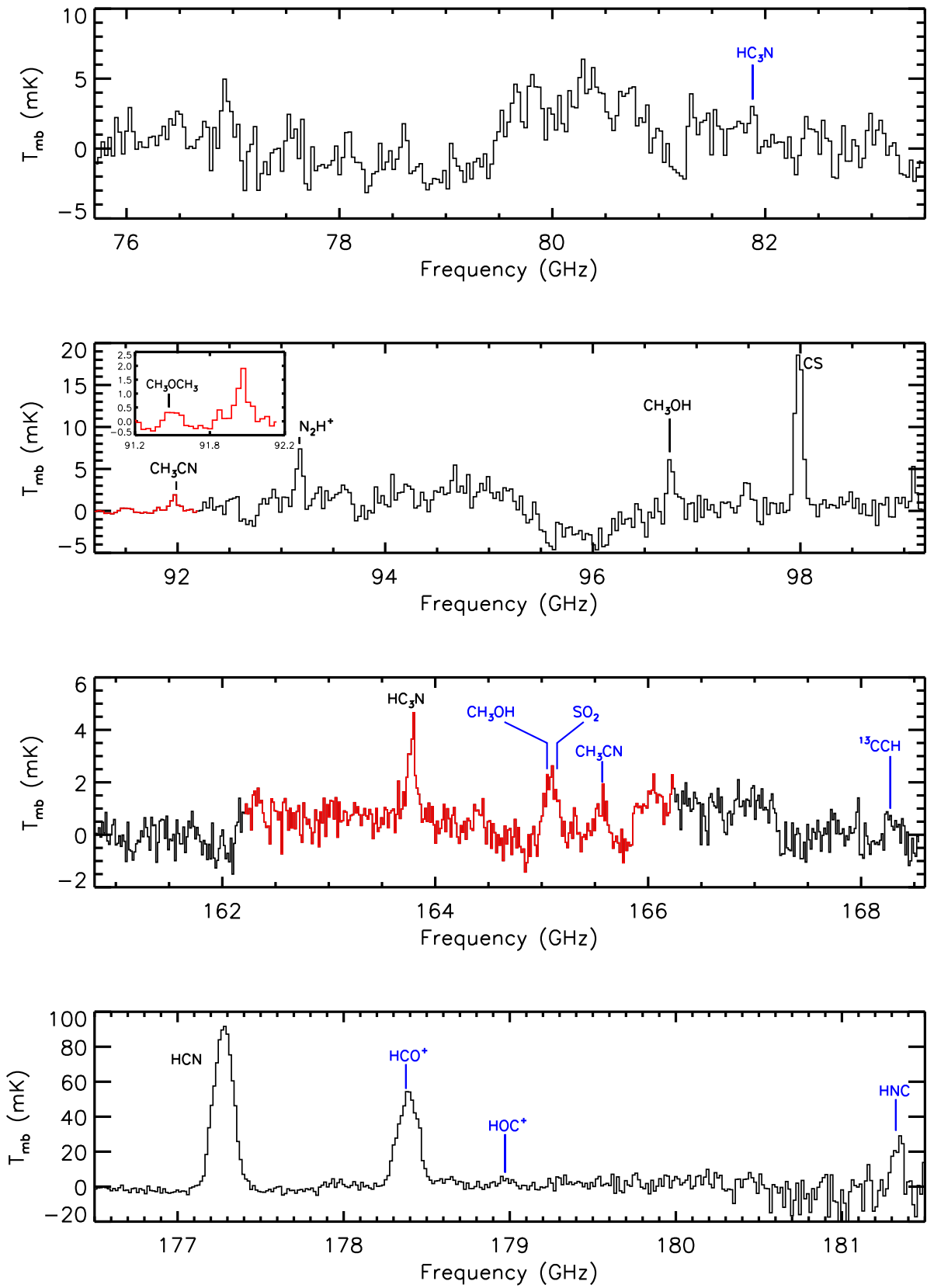


Fig. 1. Full spectra of NGC 1068 obtained in the current observations. Red represents a coaddition of the current spectrum and that in Qiu et al. (2018). Blue represents the new detections in this galaxy.

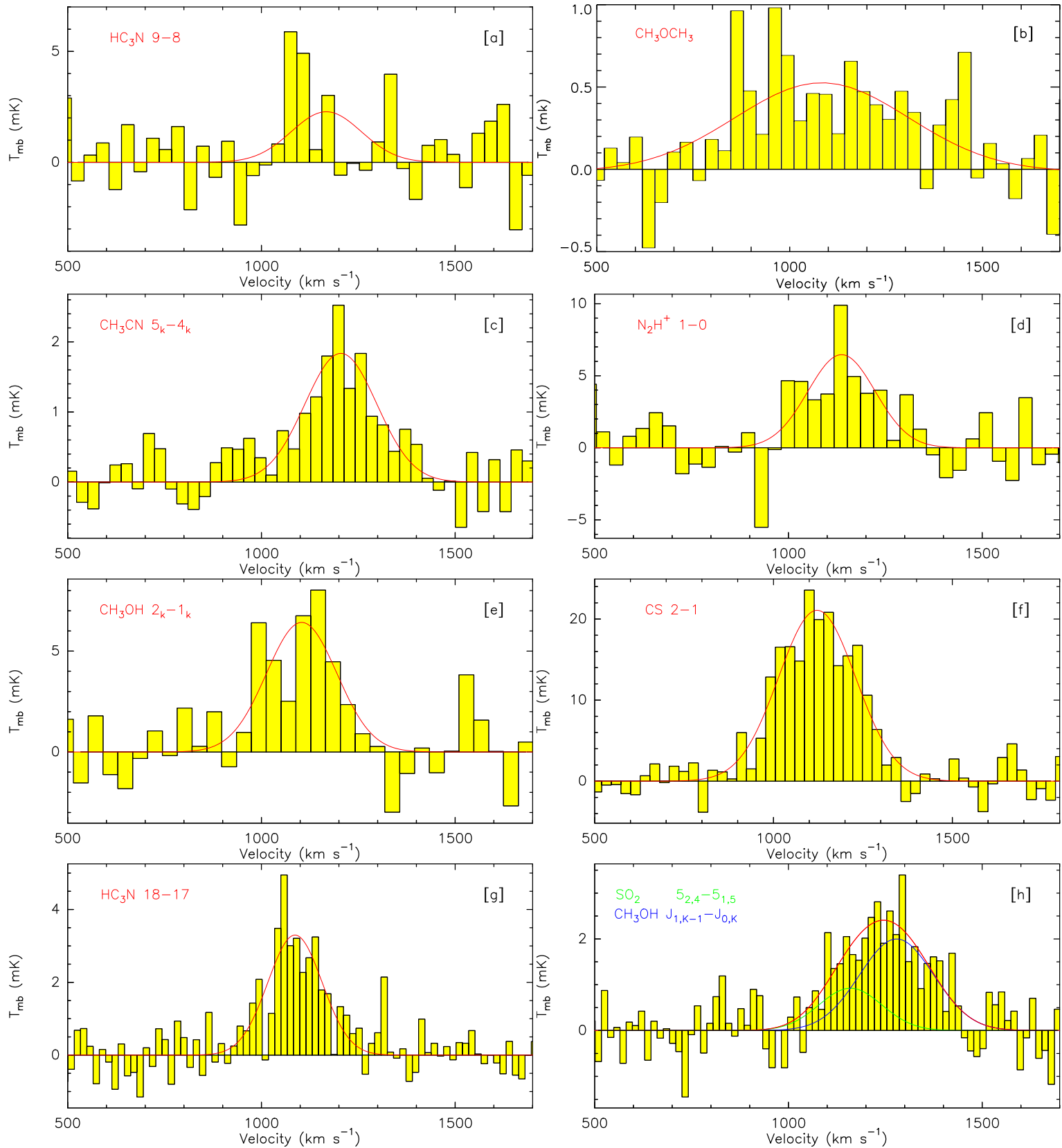


Fig. 2. Molecular transitions toward NGC 1068. The red curves represent Gaussian fitting profiles.

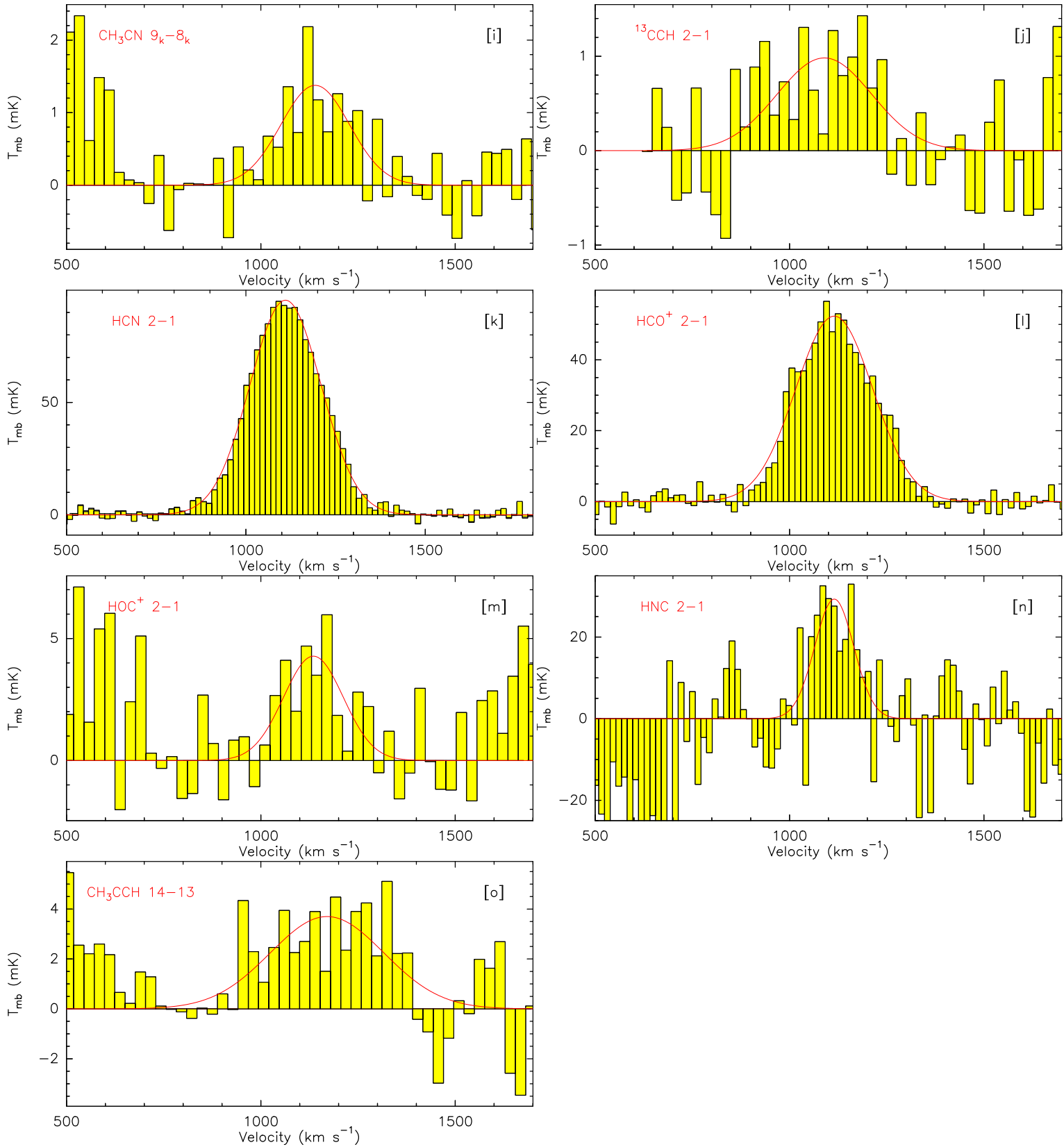


Fig. 2. continued.

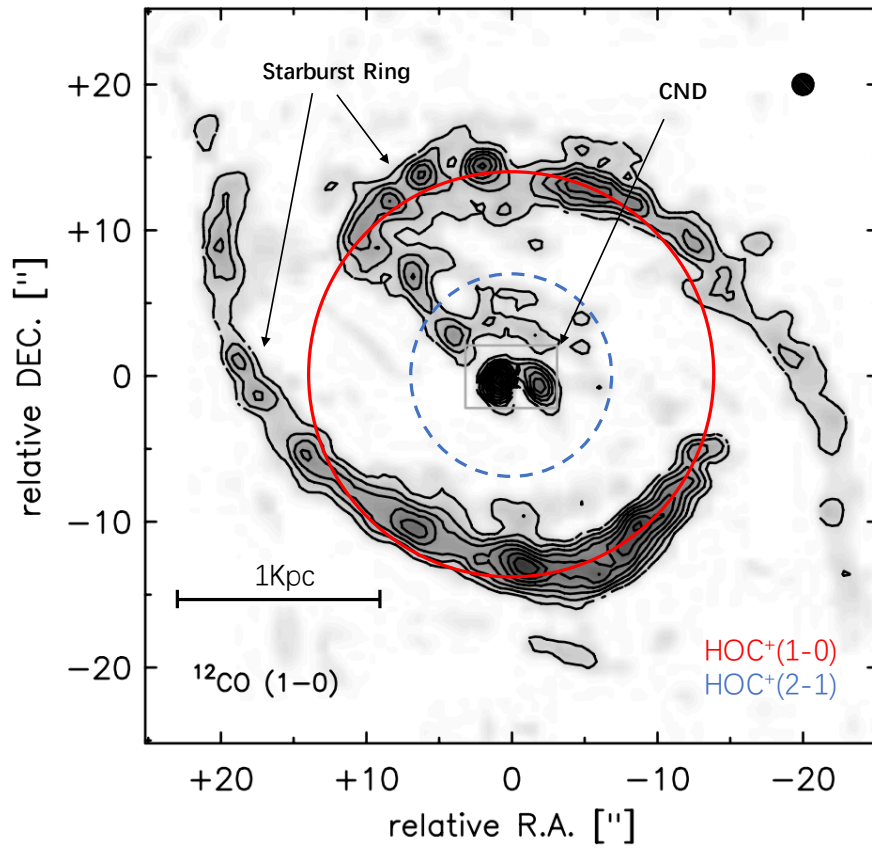


Fig. 3. CO(1 – 0) emission of NGC 1068 (gray scale and contours; taken from Schinnerer et al. (2000)). The solid and dashed circles represent the beams of HOC⁺(1 – 0) and HOC⁺(2 – 1), respectively. The central box marks the circumnuclear disk.

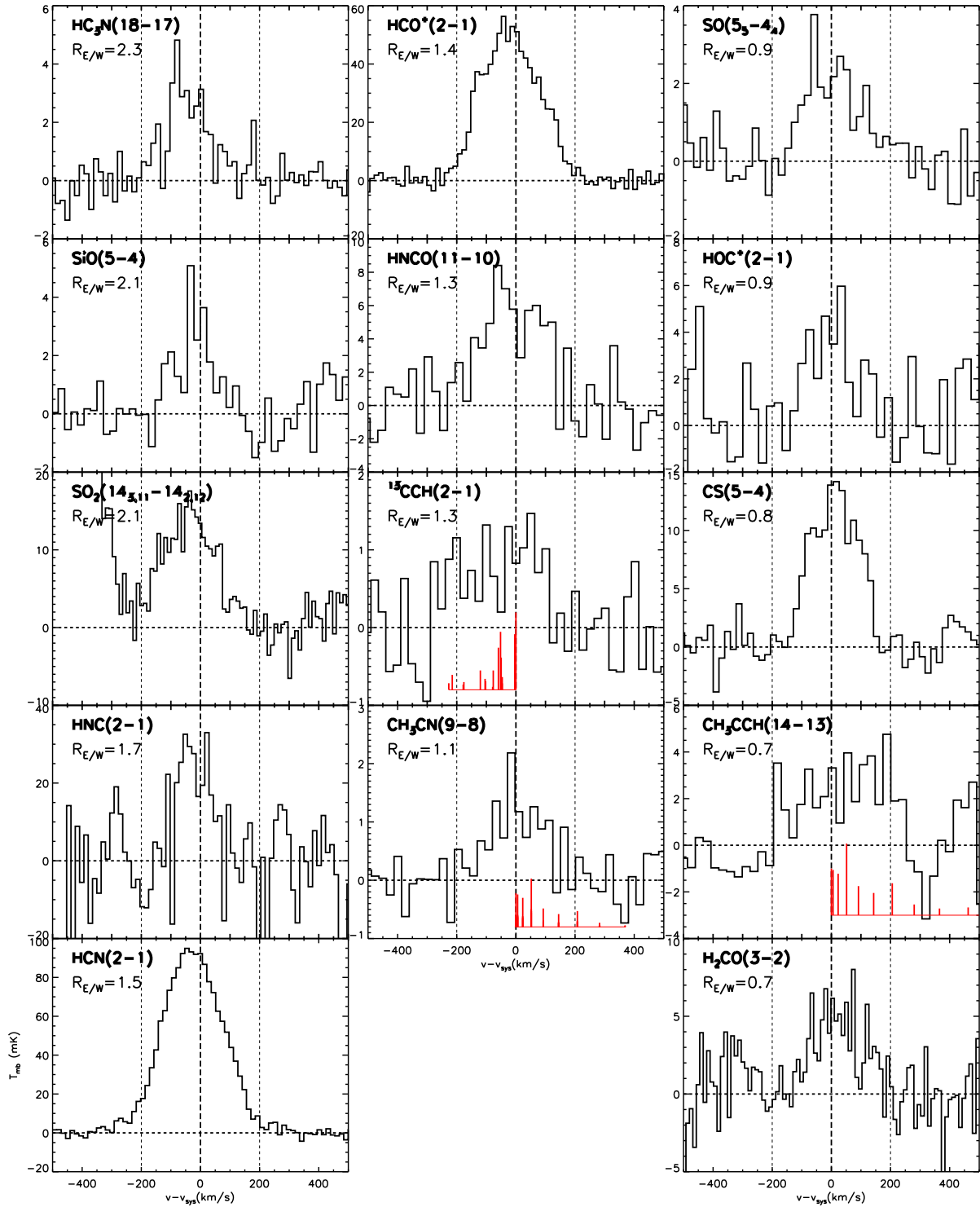


Fig. 4. Profiles of the molecular lines at 1 mm and 2 mm bands, as detected in Qiu et al. (2018) and in the current observations. The three vertical dotted lines at $v - v_{\text{sys}} = -200 \text{ km s}^{-1}$, $v - v_{\text{sys}} = 0 \text{ km s}^{-1}$, and $v - v_{\text{sys}} = +200 \text{ km s}^{-1}$ delimit the blue and red kinematical components. The wavelengths and relative intensities of the split components of $^{13}\text{CCH}(2-1)$, $\text{CH}_3\text{CN}(9-8)$, and $\text{CH}_3\text{CCH}(14-13)$ are marked by red lines.

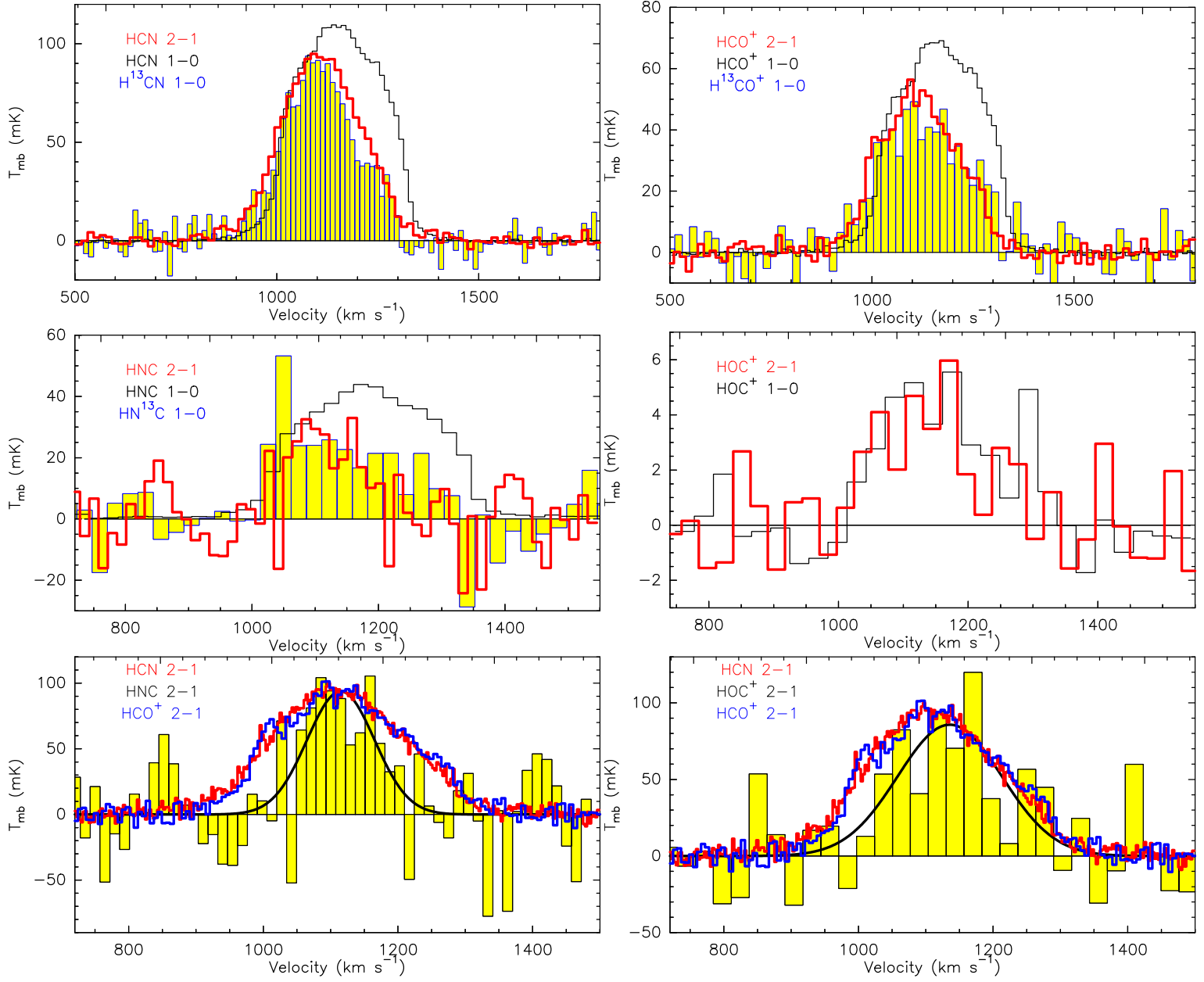


Fig. 5. Upper left panel: HCN (2-1) (red line); H^{13}CN (1-0) (blue line filled yellow, $\times 16$); HCN (1-0) (black line, $\times 1.5$). Upper right panel: HCO^+ (2-1), H^{13}CO^+ (1-0) $\times 18$, HCO^+ (1-0) $\times 1.3$. Middle left panel: HNC (2-1), HN^{13}C (1-0) $\times 35$, HNC (1-0) $\times 1.5$. Middle right panel: HOC^+ (2-1), HOC^+ (1-0) $\times 4$. Lower left panel: HCN (2-1) (red line, $\times 3.2$); HNC (2-1) (black line filled yellow, $\times 16$); HCO^+ (2-1) (black line, $\times 1.8$); the black line curve is the Gaussian fitting line of HNC (2-1). Lower right panel: HCN (2-1) (red line); HOC^+ (2-1) (black line filled yellow, $\times 20$); HCO^+ (2-1) (black line, $\times 1.8$); the black line curve is the Gaussian fitting line of HOC^+ (2-1).

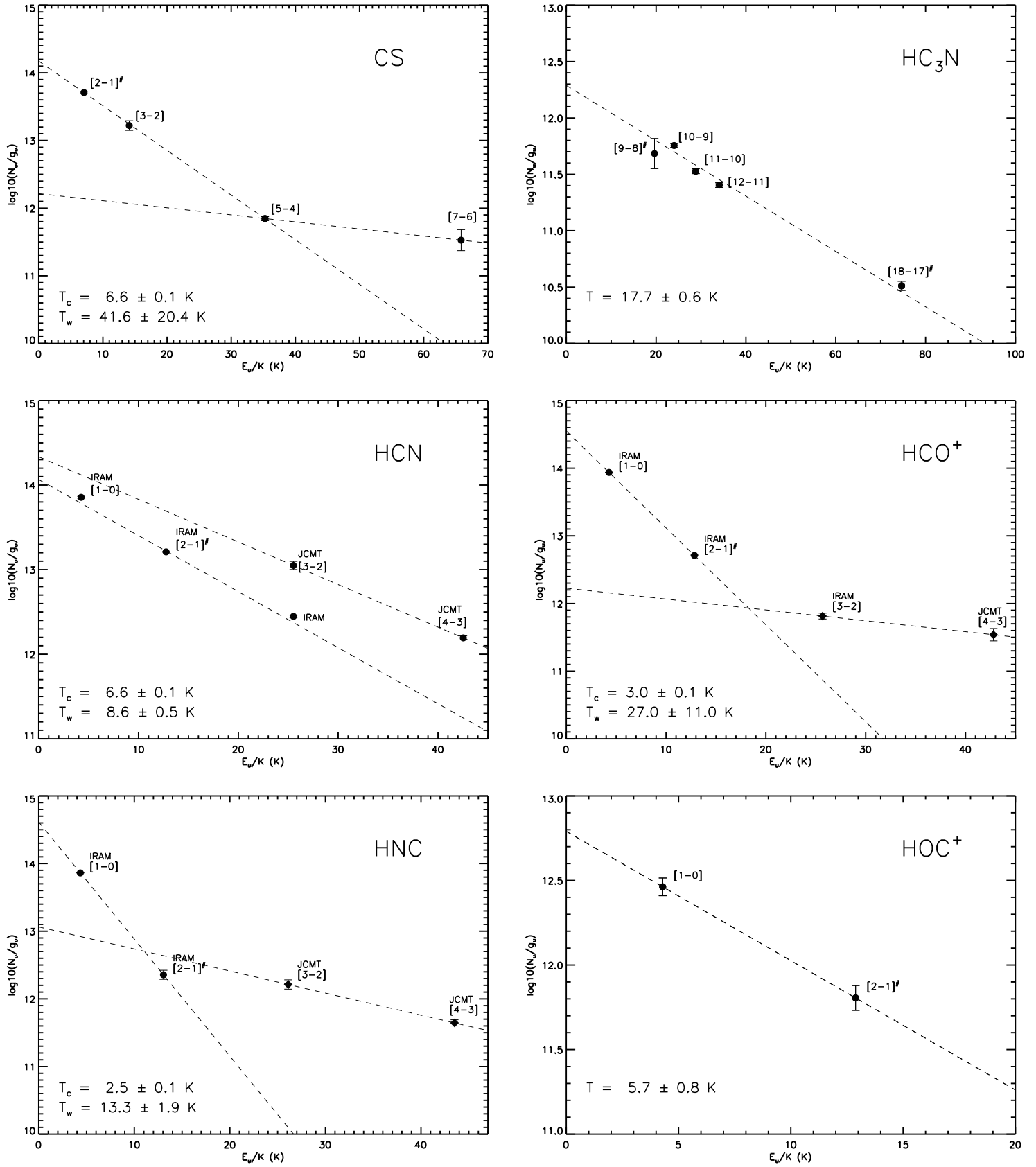


Fig. 6. Boltzmann diagrams. T_c is the rotation temperature of its cold component, and T_w is the rotation temperature of its warmer component. Transitions detected by the JCMT 15m telescope are also marked in the panels (filled diamond). The empty circles are discarded for the linear fitting. Pound signs mark the lines that are detected for the first time in this work.

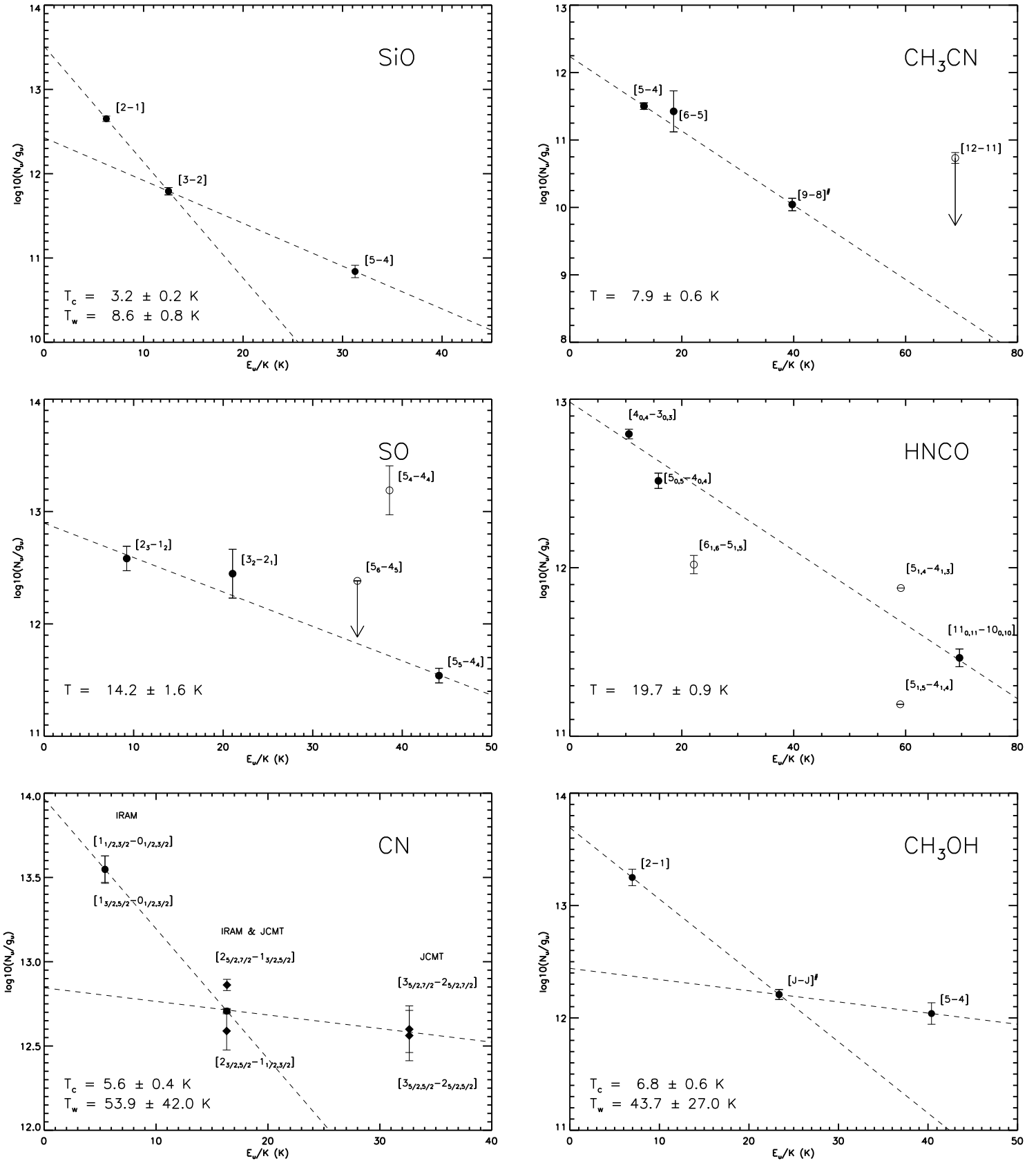


Fig. 6. continued.

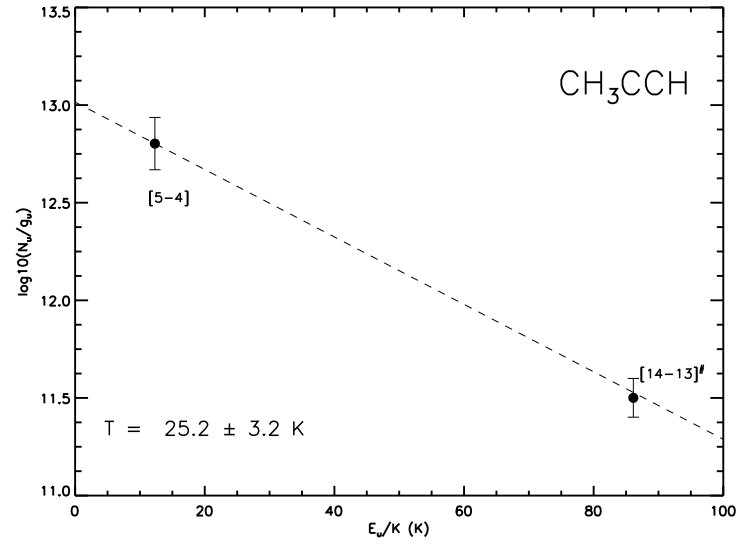
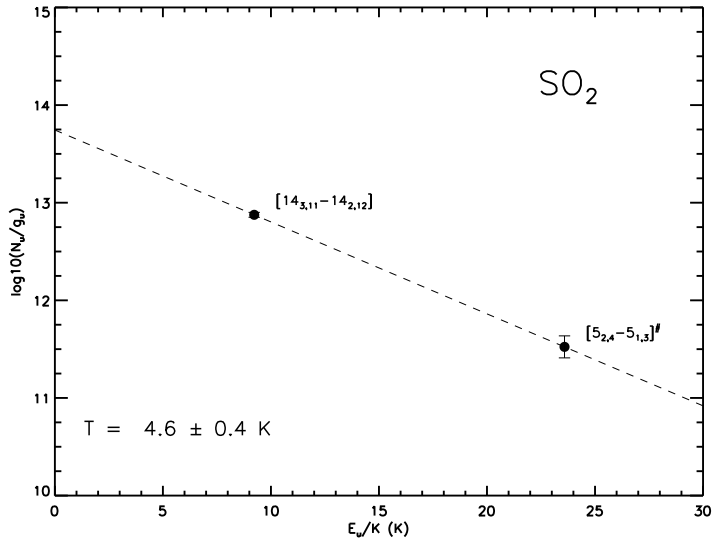


Fig. 6. continued.

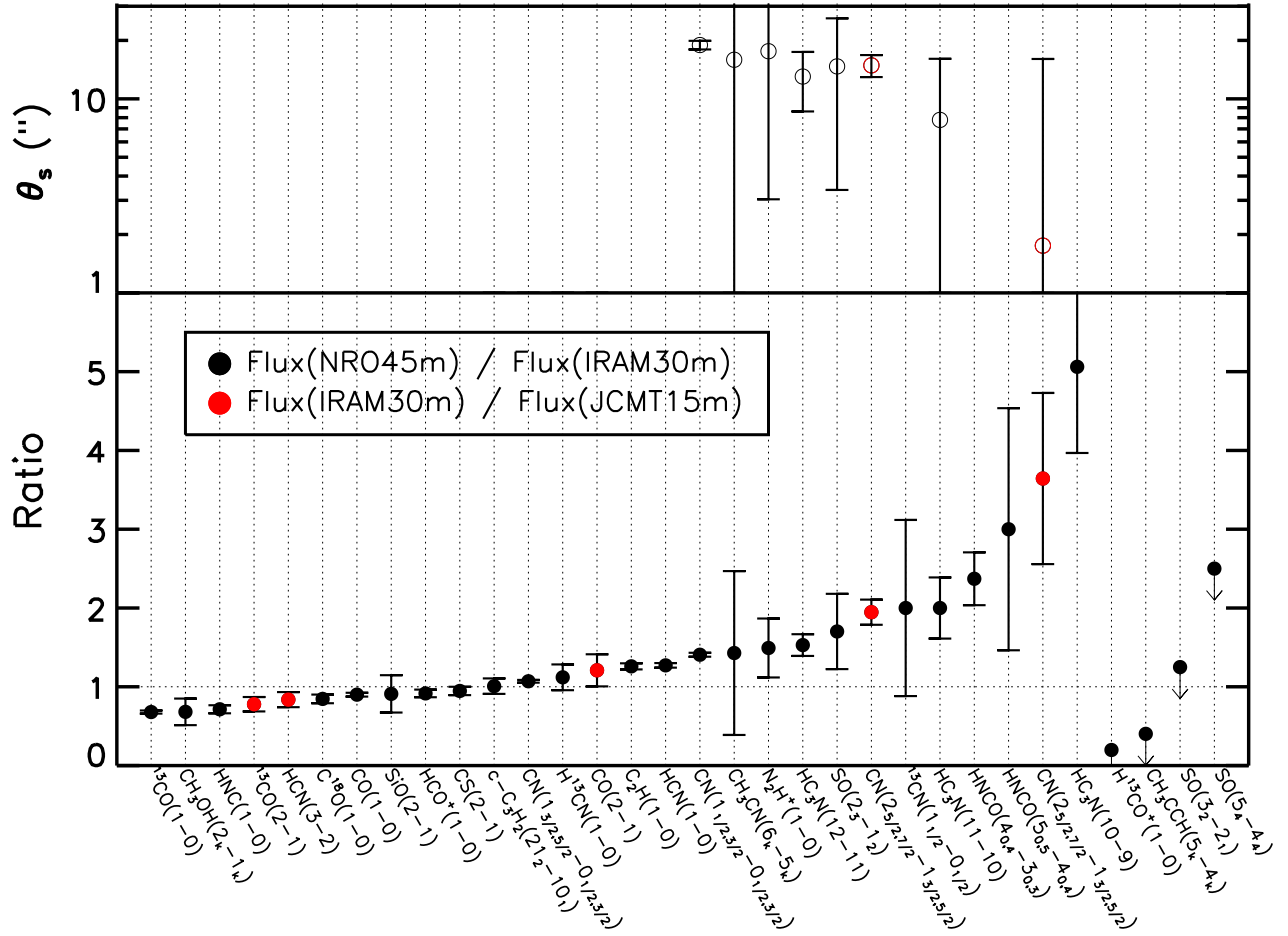


Fig. 7. Integrated intensity ratios of the molecular lines detected with different single-dish telescopes (lower panel). The calculated source sizes are shown in the upper panel.

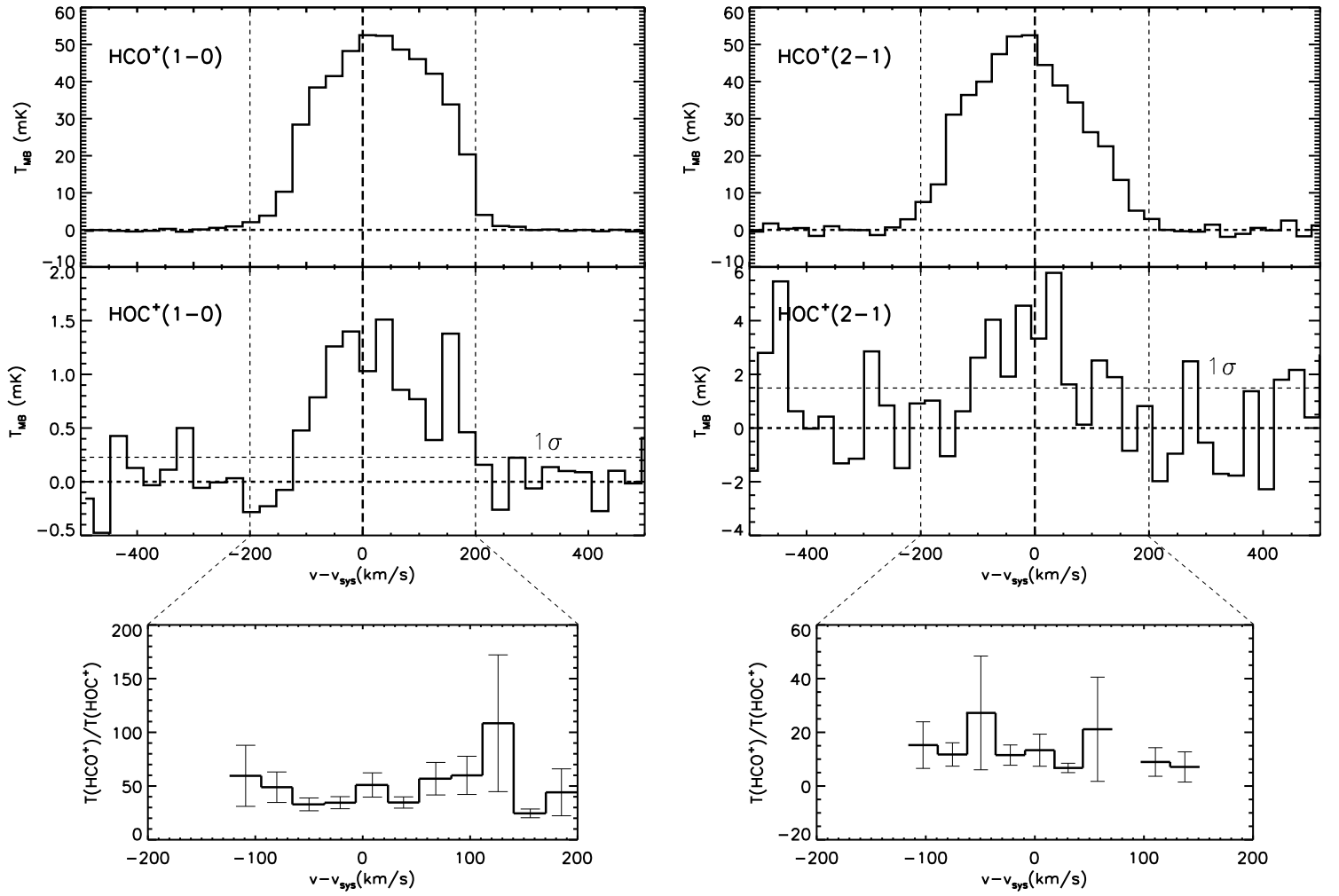


Fig. 8. Top and middle: HCO^+ and HOC^+ spectra. Bottom: HCO^+ -to- HOC^+ temperature ratio profile derived for channels fulfilling $T(\text{HOC}^+) > 1\sigma$ (left: $J = 1 - 0$ transitions; right: $J = 2 - 1$ transitions).

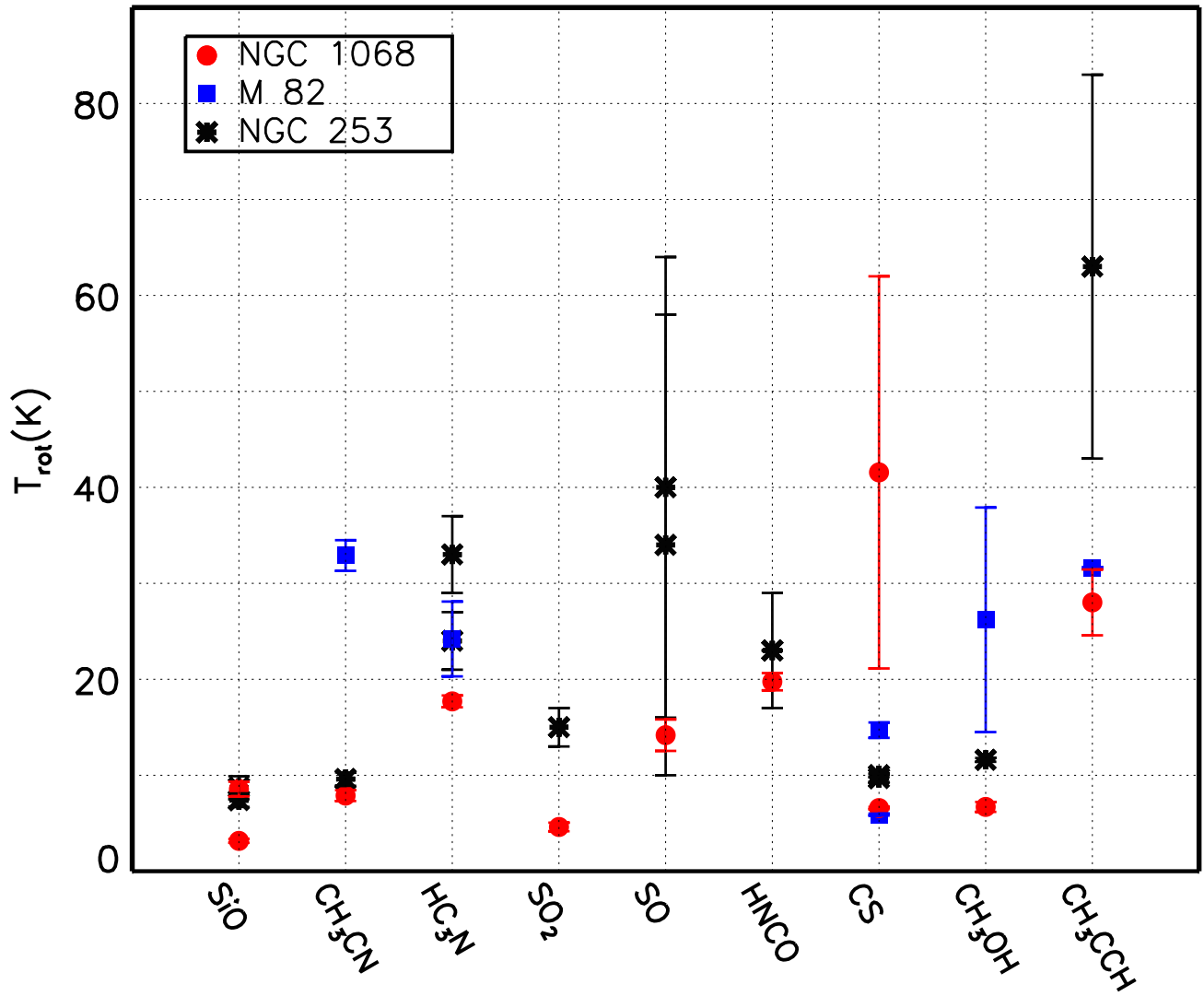


Fig. 9. Comparison of the rotation temperatures in NGC 1068, M 82, and NGC 253. The molecular rotation temperatures of M 82 and NGC 253 are taken from Aladro et al. (2011) and Martín et al. (2006).

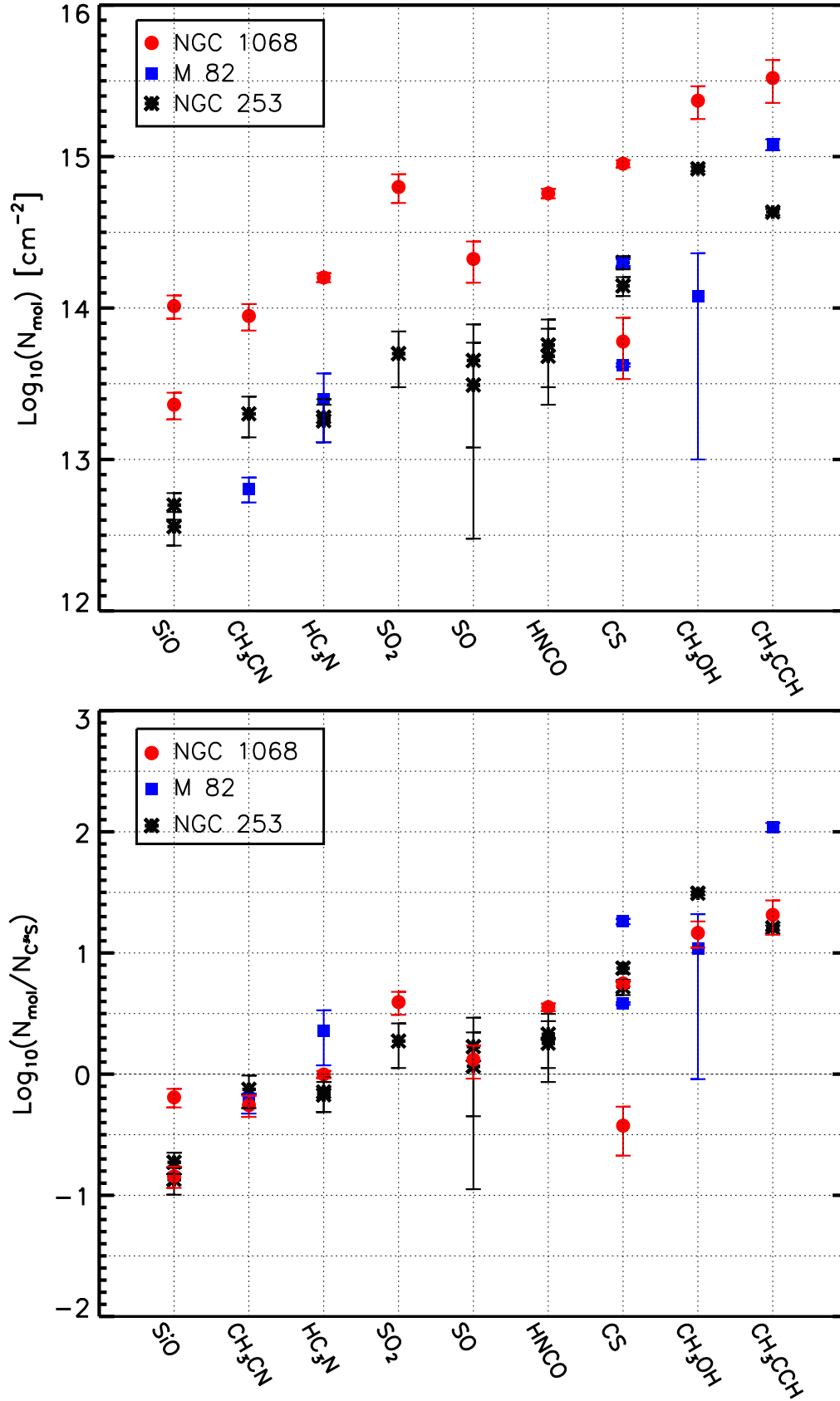


Fig. 10. Upper panel: Comparison of the column densities in NGC 1068, M 82, and NGC 253. Lower panel: Comparison of the fraction abundances with respect to C^{34}S . The column densities of the molecules in M 82 and NGC 253 are taken from Aladro et al. (2011) and Martín et al. (2006), respectively. The column density of C^{34}S in NGC 1068 is taken from Aladro et al. (2013).

Table 1. Band parameters.

band range GHz	F_{eff} %	B_{eff} %	On-time ^a hour	HPBW ^b "	spatial resolution Kpc
75.691-83.502	95	81	0.7	32.5 - 29.5	2.3 - 2.1
91.440-99.224	95	81	0.7	26.9 - 24.8	1.9 - 1.7
160.756-168.567	93	73	18.0	15.3 - 14.6	1.1 - 1.0
176.498-184.309	93	68	18.0	13.9 - 13.3	0.9

Notes. ^(a) on-source time for each band; ^(b) $\frac{\text{HPBW}}{\text{arcsec}} = \frac{2460}{\text{Freq}} \times \frac{1}{\text{GHz}}$.

F_{eff} and B_{eff} are taken from the website of the IRAM 30m (<http://www.iram.es/IRAMES/mainWiki/Iram30mEfficiencies>).

Table 2. The transitions detected with single dish telescope in NGC 1068.

Line	Frequency MHz	Flux mK km s ⁻¹	Velocity km s ⁻¹	Line Width km s ⁻¹	T_{mb} mK	RMS mK	Telescope	HPBW "	Ref.
HC ₃ N (9 – 8) ^a	81881.5	517.3 ± 160.7	1167.6	213.2	2.28	1.37	IRAM 30m	30.0	1, P
CH ₃ OH (5 _k – 4 _k)	84521.2	127.2 ± 28.0	1035.7 ± 8.9	78.0 ± 19.1	1.53	0.41	IRAM 30m	29.1	2
HC ¹⁸ O ⁺ (1 – 0)	85162.2	125.6 ± 40.3	1124.7 ± 58.3	317.6 ± 107.9	0.37	0.27	IRAM 30m	28.9	2
c-C ₃ H ₂ (2 _{1,2} – 1 _{0,1})	85338.9	133.1 ± 36.8	1124.5 ± 49.5	300.8 ± 83.3	IRAM 30m	28.9	5
		1190.3 ± 59.9	1128.6 ± 6.3	249.6 ± 12.4	4.48	0.36	IRAM 30m	28.8	2
		1200 ± 100	1148 ± 17	176 ± 40	5	1	NRO 45m	19.0	3
		1200	1148	248	5	1.7	NRO 45m	19.0	4
CH ₃ CCH (5 _k – 4 _k)	85457.3	347.5 ± 107.2	1126.0 ± 42.4	363.8 ± 156.7	0.90	0.36	IRAM 30m	28.8	2
		< 140	NRO 45m	19.0	3
H42 α	85695.0	448.2 ± 77.7	1251.0 ± 28.3	377.1 ± 91.9	1.12	0.43	IRAM 30m	28.7	2
HC ¹⁵ N (1 – 0)	86055.0	< 115(2 σ)	IRAM 30m	28.6	5
H ¹³ CN (1 – 0)	86340.2	1249.8 ± 37.2	1109.6 ± 3.1	211.9 ± 7.3	5.54	0.45	IRAM 30m	28.5	2
		1400 ± 200	1126 ± 9	196 ± 20	7	1	NRO 45m	18.7	3
		1900	1111	234	9	4.1	NRO 45m	18.7	4
		1282.3 ± 33.5	1109.3 ± 2.7	215.6 ± 6.5	IRAM 30m	28.5	5
		400	1066.3	166.4	2.4	...	IRAM 30m	28.5	6
		780 ± 80	1088.4 ± 11.2	180	4.03	...	IRAM 30m	28.5	7
		1400 ± 200	7	1	NRO 45m	18.7	8
		1556 ± 617	...	230 ± 33	IRAM 30m	28.5	9
		HCO (1 _{0,1} – 0 _{0,0})	86670.8	376.9 ± 107.6	1186.4 ± 38.7	293.8 ± 86.4	1.21	0.37	IRAM 30m
		200	1100	240	0.6	...	IRAM 30m	28.4	6
		490 ± 120	1100	240	1.08	...	IRAM 30m	28.4	7
H ¹³ CO ⁺ (1 – 0)	86754.3	758.2 ± 38.7	1127.8 ± 6.9	275.5 ± 16.0	2.60	0.31	IRAM 30m	28.4	2
		< 150	NRO 45m	18.7	3
		734.4 ± 38.27	1124.9 ± 6.9	270.5 ± 15.8	IRAM 30m	28.4	5
		500	1100	240.0	1.9	...	IRAM 30m	28.4	6
		741 ± 617	...	230 ± 33	IRAM 30m	28.4	9
		570 ± 70	1128 ± 13	254 ± 38	2.1	...	IRAM 30m	28.4	10
SiO (2 – 1)	86847.0	878.9 ± 64.5	1101.1 ± 7.8	248.5 ± 21.5	3.32	0.37	IRAM 30m	28.3	2
		800 ± 200	1092 ± 19	176 ± 46	5	1	NRO 45m	18.7	3
		600	1100	259.1	2.2	...	IRAM 30m	28.3	6
		600 ± 70	1100	240	2.36	...	IRAM 30m	28.3	7
		800 ± 200	5	1	NRO 45m	18.7	8
		988 ± 617	...	230 ± 33	IRAM 30m	28.3	9
		560 ± 50	1111 ± 10	189 ± 22	2.8	...	IRAM 30m	28.3	10
		IRAM 30m	28.3	5
HC ¹⁷ O ⁺ (1 – 0)	87057.3	< 144(2 σ)	IRAM 30m	28.3	5
HN ¹³ C (1 – 0)	87091.0	251.5 ± 24.1	1126.9 ± 12.2	243.6 ± 24.6	0.97	0.29	IRAM 30m	28.2	2
		204.2 ± 28.5	1117.5 ± 16.2	216.3 ± 30.8	IRAM 30m	28.2	5
		200 ± 300	1075.7 ± 124.4	151.8 ± 235.9	1.1	...	IRAM 30m	28.2	6
		190 ± 50	1100	150	1.20	...	IRAM 30m	28.2	7
C ₂ H (1 – 0)	87316.9	7940.2 ± 53.0	1073.8 ± 1.4	445.0 ± 3.4	16.83	0.46	IRAM 30m	28.2	2
		4400 ± 300	1117 ± 11	187 ± 24	20	2	NRO 45m	19.0	3 ^b
		2600 ± 300	1110 ± 31	313 ± 80	9	1
		6900	1139	209	19	3.3	NRO 45m	19.0	4
		3100	1098.4	240.0	12.0	...	IRAM 30m	28.2	6
		7800 ± 100	1106.4 ± 2.6	239.8 ± 5.3	18.51	...	IRAM 30m	28.2	7
		10000 ± 2200	...	471 ± 33	IRAM 30m	28.2	9
HNCO (4 _{0,4} – 3 _{0,3})	87925.2	674.8 ± 44.6	1148.0 ± 9.0	272.9 ± 20.6	2.32	0.27	IRAM 30m	28.0	2
		1600 ± 200	1134 ± 57	250 ± 134	6	3	NRO 45m	19.1	3
		100	1100	230	0.4	...	IRAM 30m	28.0	6
		570 ± 890	1100	240	2.20	...	IRAM 30m	28.0	7
		1600 ± 200	6	3	NRO 45m	19.1	8
HCN (1 – 0)	88631.8	20754.0 ± 28.8	1155.6 ± 0.2	250.3 ± 0.4	77.91	0.44	IRAM 30m	28.0	2
		26400 ± 600	1117 ± 3	233 ± 6	108	2	NRO 45m	19.1	3
		35000	1117	336	128	19.1	NRO 45m	19.1	4
		20578.6 ± 44.9	1150.8 ± 0.2	249.3 ± 0.5	IRAM 30m	28.0	5
		11100	1120.1	238.5	43.0	...	IRAM 30m	28.0	6
		23550 ± 280	1112.8 ± 1.6	215.9 ± 3.4	77.84	...	IRAM 30m	28.0	7
		26400 ± 600	108	2	NRO 45m	19.1	8
		27000 ± 500	...	241 ± 33	IRAM 30m	28.0	9

		24500 ± 900	...	220 ± 10	IRAM 30m	28.0	11
H ¹⁵ NC (1 – 0)	88865.7	< 112(2σ)	IRAM 30m	27.7	5
HCO ⁺ (1 – 0)	89188.5	14519.0 ± 56.0	1167.6 ± 0.5	245.0 ± 1.0	55.66	0.89	IRAM 30m	27.6	2
		13300 ± 700	1132 ± 5	236 ± 11	55	2	NRO 45m	19.1	3
		14430.9 ± 66.5	1167.7 ± 0.6	244.1 ± 1.2	IRAM 30m	27.6	5
		13800 ± 300	1122.6 ± 1.2	230.9 ± 1.5	55.9	...	IRAM 30m	27.6	6
		14360 ± 170	1113.7 ± 1900	219.3 ± 4.2	56.30	...	IRAM 30m	27.6	7
		13300 ± 700	55	2	NRO 45m	19.1	8
		18148 ± 493	...	232 ± 33	IRAM 30m	27.6	9
		14600 ± 200	...	234 ± 4	IRAM 30m	27.6	11
HOC ⁺ (1 – 0)	89487.4	248.1 ± 31.9	1154.2 ± 13.5	192.8 ± 26.8	1.21	0.30	IRAM 30m	27.5	2
		200 ± 100	1173.3 ± 17.5	128.2 ± 51.6	1.8	...	IRAM 30m	27.5	6
		310 ± 60	1110	234.1 ± 73.4	1.23	...	IRAM 30m	27.5	7
HNC (1 – 0)	90663.6	7835.6 ± 35.0	1185.9 ± 0.6	244.3 ± 1.2	30.10	0.39	IRAM 30m	27.1	2
		5600 ± 400	1138 ± 7	200 ± 17	28	2	NRO 45m	19.1	3
		7781.6 ± 35.5	1186.0 ± 0.6	243.5 ± 30.0	IRAM 30m	27.1	5
		7500 ± 600	1141.3 ± 0.3	235.9 ± 3.2	30.8	...	IRAM 30m	27.1	6
		7780 ± 100	1112.2 ± 1.9	225.1 ± 4.4	31.12	...	IRAM 30m	27.1	7
		5600 ± 400	28	2	NRO 45m	19.1	8
		11000 ± 500	...	238 ± 33	IRAM 30m	27.1	9
		4324 ± 676	1073 ± 13	114 ± 30	13.1	2.4	SEST 15m	55	12 ^b
			1268 ± 20	170 ± 62	9.1	2.0			
		11400 ± 700	1137 ± 7	232 ± 17	46	...	IRAM 30m	25	13
HC ₃ N (10 – 9)	90979.0	928.5 ± 35.5	1167.6 ± 4.1	213.2 ± 9.3	4.09	0.31	IRAM 30m	27.0	2
		4700 ± 1000	1078 ± 33	254 ± 77	16	4	NRO 45m	19.1	3
		1100 ± 100	1142.6 ± 10.0	263.7 ± 24.9	3.8	...	IRAM 30m	27.0	6
		710 ± 30	1091.0 ± 5.6	190	3.52	...	IRAM 30m	27.0	7
		4700 ± 1000	16	4	NRO 45m	19.1	8
		1200 ± 450	...	251 ± 33	IRAM 30m	27.0	9
CH ₃ OCH ₃ (3 _{2,2} – 3 _{1,3})	91476.6	305.7 ± 129.0	1083.2 ± 110.8	565.3 ± 181.6	0.54	0.23	IRAM 30m	26.9	1, A
		224.8 ± 52.2	1060.6 ± 49.7	410.3 ± 100.1	0.52	0.33	IRAM 30m	26.9	2
CH ₃ CN (5 _k – 4 _k)	91987.1	427.4 ± 48.6	1205.2 ± 11.1	218.7 ± 33.6	1.84	0.35	IRAM 30m	26.7	1, C
		395.3 ± 43.8	1196.7 ± 10.2	203.5 ± 29.6	1.82	0.35	IRAM 30m	26.7	2
		100	1100	150.0	0.6	...	IRAM 30m	26.7	6
		590 ± 420	1100	240	2.30	...	IRAM 30m	26.7	7
N ₂ H ⁺ (1 – 0)	93173.4	1407.0 ± 229.3	1137.3 ± 17.1	204.7 ± 35.8	6.46	1.91	IRAM 30m	26.4	1, P
		2100 ± 400	1112 ± 16	245 ± 37	8	1	NRO 45m	19.1	3
		1000	1164.1	233.5	4.0	...	IRAM 30m	26.4	6
		1990 ± 80	1100.6 ± 5.4	240	7.62	...	IRAM 30m	26.4	7
C ³⁴ S (2 – 1)	96412.9	700 ± 100	1091.2 ± 15.7	249.0 ± 29.5	2.7	...	IRAM 30m	25.5	6
		680 ± 80	1100	240	2.64	...	IRAM 30m	25.5	7
		< 330	NRO 45m	19	8
CH ₃ OH (2 _k – 1 _k)	96741.4	1613.3 ± 271.4	1104.2 ± 20.0	225.9 ± 42.1	6.71	1.92	IRAM 30m	25.4	1, P
		1100 ± 200	1104 ± 16	225 ± 40	5	1	NRO 45m	19.0	3
		1500	1104	235	7	3.8	NRO 45m	19.0	4
		900	1117.5	247.2	3.3	...	IRAM 30m	25.4	6
		1550 ± 90	1100	240	5.93	...	IRAM 30m	25.4	7
		1100 ± 200	5	1	NRO 45m	19.0	8
CS (2 – 1)	97981.0	5700.7 ± 239.0	1121.9 ± 5.4	254.1 ± 11.7	21.08	1.95	IRAM 30m	25.1	1, P
		5400 ± 200	1123 ± 5	242 ± 12	22	1	NRO 45m	19.0	3
		6400	1174	312	30	4.8	NRO 45m	19.0	4
		3950 ± 90	1092.8 ± 3.3	212.2 ± 7.6	17.14	...	IRAM 30m	25.1	7
		5400 ± 200	22	1	NRO 45m	19.0	8
SO (2 ₃ – 1 ₂)	99299.9	800 ± 200	1194 ± 26	219 ± 62	4	1	NRO 45m	16.5	3
		400 ± 100	1111.1 ± 7.5	136.0 ± 17.0	3.1	...	IRAM 30m	24.8	6
		470 ± 60	1065.1 ± 12.4	139.7 ± 29.0	3.13	...	IRAM 30m	24.8	7
		800 ± 200	4	1	NRO 45m	16.5	8
SO (5 ₄ – 4 ₄)	100029.6	200 ± 100	1111.1	136.0	1.6	...	IRAM 30m	24.6	6
		< 400	NRO 45m	16.5	8
HC ₃ N (11 – 10)	100076.4	1600 ± 300	1094 ± 19	171 ± 46	9	2	NRO 45m	16.5	3
		500	1142.6	263.0	2.0	...	IRAM 30m	24.6	6
		800 ± 40	1091.0 ± 5.6	190	3.95	...	IRAM 30m	24.6	7
		1600 ± 300	9	2	NRO 45m	16.5	8
¹³ CN (1 _{1,0} – 0 _{1,1})	108426.9	100	1104	257.2	0.2	...	IRAM 30m	22.7	6

$^{13}\text{CN}(1_{1/2} - 0_{1/2})$	108651.3	400 \pm 100	1076 \pm 21	191 \pm 50	2	1	NRO 45m	16.5	3
		200	1104	257.2	0.6	...	IRAM 30m	22.6	6
$^{13}\text{CN}(1_{3/2} - 0_{1/2})$	108780.2	500 \pm 100	1099 \pm 21	197 \pm 50	3	1	NRO 45m	16.5	3
$\text{HC}_3\text{N}(12 - 11)$	109173.6	1300 \pm 100	1103 \pm 16	229 \pm 36	5	1	NRO 45m	16.5	3
		700	1142.6	263.0	2.6	...	IRAM 30m	22.5	6
		850 \pm 40	1091.0 \pm 5.6	190	4.19	...	IRAM 30m	22.5	7
		1300 \pm 100	5	1	NRO 45m	16.5	8
$\text{SO}(3_2 - 2_1)$	109252.2	200 \pm 100	1111.1	136.0	1.3	...	IRAM 30m	22.5	6
		< 250	NRO 45m	16.5	8
		40	1100	230.0	0.2	...	IRAM 30m	22.5	6
$\text{HNCO}(5_{1,5} - 4_{1,4})$	109496.0	3300 \pm 200	1127 \pm 10	320 \pm 24	11	1	NRO 45m	16.5	3
$\text{C}^{18}\text{O}(1 - 0)$	109782.2	3600 \pm 200	1142.2 \pm 6.1	230.0	13.0	...	IRAM 30m	22.4	6
		3900 \pm 90	1100.5 \pm 4.0	258.0 \pm 9.4	14.02	...	IRAM 30m	22.4	7
		3300 \pm 200	11	1	NRO 45m	16.5	8
		4450 \pm 120	1102 \pm 4	264 \pm 8	15.8	0.8	IRAM 30m	22.4	14
		900 \pm 100	1133 \pm 15	209 \pm 48	4	1	NRO 45m	16.5	3
$\text{HNCO}(5_{0,5} - 4_{0,4})$	109905.8	300	1100	230.0	1.3	...	IRAM 30m	22.4	6
		900 \pm 100	4	1	NRO 45m	16.5	8
		860 \pm 90	1086 \pm 11	210 \pm 20	3.9	0.8	IRAM 30m	22.4	14
		8900 \pm 200	1143 \pm 5	241 \pm 11	36	1	NRO 45m	16.5	3
$^{13}\text{CO}(1 - 0)$	110201.4	12800 \pm 700	1105.2 \pm 3.6	252.1 \pm 4.9	45.8	...	IRAM 30m	22.3	6
		13100 \pm 240	1100.8 \pm 2.9	237.6 \pm 5.8	49.36	...	IRAM 30m	22.3	7
		8900 \pm 200	36	1	NRO 45m	16.5	8
		15200 \pm 1800	51	...	IRAM 30m	21	15
		200	1100	230	0.7	...	IRAM 30m	22.3	6
$\text{HNCO}(5_{1,4} - 4_{1,3})$	110298.1	1000 \pm 200	1123 \pm 31	287 \pm 73	3	1	NRO 45m	16.5	3
		100	1100.0	150.0	0.8	...	IRAM 30m	22.3	6
		700 \pm 490	1100	240	2.71	...	IRAM 30m	22.3	7
		1000 \pm 200	3	1	NRO 45m	16.5	8
$\text{C}^{17}\text{O}(1 - 0)$	112359.0	~ 5	...	NRO 45m	15.2	3
$\text{CN}(1_{1/2,3/2} - 0_{1/2,3/2})$	113191.3	18500 \pm 300	1191 \pm 3	275 \pm 7	63	1	NRO 45m	15.2	3
		4500	1152.8	247.4	17.3	...	IRAM 30m	21.7	6
		13150 \pm 100	1114.0 \pm 1.0	224.4 \pm 2.5	43.20	...	IRAM 30m	21.7	7
		136 \pm 54	22.0	13.4	SEST 15m	45	12 ^b
$\text{CN}(1_{3/2,5/2} - 0_{1/2,3/2})$	113491.0	27600 \pm 400	1191 \pm 2	239 \pm 5	110	2	NRO 45m	15.2	3
		12100	1152.8	247.4	46.0	...	IRAM 30m	21.7	6
		25790 \pm 190	1110.4 \pm 1.0	224.4 \pm 2.5	87.19	...	IRAM 30m	21.7	7
		46100 \pm 500	110	2	NRO 45m	15.2	8
		94 \pm 42	18.0	18.6	SEST 15m	45	12 ^b
$\text{C}^{34}\text{S}(3 - 2)$	114617.1	530 \pm 120	1070 \pm 30	230 \pm 60	2.2	1.0	IRAM 30m	21.5	14
		400	1100	140	2.8	...	IRAM 30m	21.4	6
$\text{NS}(3_1 - 2_1)$	115153.9	155000 \pm 1000	1143 \pm 3	237 \pm 7	638	16	NRO 45m	15.2	3
		172200 \pm 4500	1168.3 \pm 0.3	251.5 \pm 0.4	618.0	...	IRAM 30m	21.3	6
		81300 \pm 1010	1168.1 \pm 10.2	122.5 \pm 10.8	624.39	...	IRAM 30m	21.3	7
		155000 \pm 1000	638	16	NRO 45m	15.2	8
		177000 \pm 21000	IRAM 30m	21	15
$\text{CO}(1 - 0)$	115271.2	162429 \pm 16285	1007 \pm 1	58 \pm 3	321.7	21.3	SEST 15m	44	12 ^c
		...	1100 \pm 3	156 \pm 11	378.7	5.4
		...	1234 \pm 2	96 \pm 4	37.6	15.4
$\text{NS}(3_1 - 2_1)$	115556.2	400	1100	140	2.8	...	IRAM 30m	21.3	6
$\text{SiO}(3 - 2)$	130268.7	600 \pm 60	1101 \pm 10	190 \pm 19	3.0	...	IRAM 30m	18.9	10
$\text{HNCO}(6_{1,6} - 5_{1,5})$	131885.7	560 \pm 70	1114 \pm 13	210 \pm 30	2.5	0.6	IRAM 30m	18.7	14
$\text{CS}(3 - 2)$	146969.0	9100 \pm 1500	1100	245	30.0	10.0	IRAM 30m	16.7	16
$\text{HC}_3\text{N}(18 - 17)$	163753.4	578.9 \pm 49.2	1086.8 \pm 6.5	164.9 \pm 18.1	3.30	0.54	IRAM 30m	15.0	1, C
$\text{CH}_3\text{OH}(J_{1,j-1} - J_{0,j})\text{E}^d$	165061.2	551.5 \pm 47.0	1137.0	225.9	2.29	0.59	IRAM 30m	14.9	1, C
$\text{SO}_2(5_{2,4} - 5_{1,5})^d$	165144.6	145.9 \pm 43.2	1097.9	191.1	0.72	0.59	IRAM 30m	14.9	1, C
$\text{CH}_3\text{CN}(9_k - 8_k)$	165569.1	213.6 \pm 63.0	1145.2 \pm 26.4	169.6 \pm 35.3	1.18	0.63	IRAM 30m	14.9	1, C
$^{13}\text{CCH}(2 - 1)$	168274.5	300.6 \pm 70.0	1089.7 \pm 36.2	287.6 \pm 62.1	0.98	0.58	IRAM 30m	14.6	1, P
$\text{HCN}(2 - 1)$	177238.7	23609.0 \pm 173.0	1072.4 \pm 0.8	232.7 \pm 2.0	95.32	2.05	IRAM 30m	13.9	1, P
		20000 \pm 400	...	220 \pm 10	IRAM 30m	13.9	11
$\text{HCO}^+(2 - 1)$	178375.1	12976.0 \pm 183.6	1116.1 \pm 1.7	233.5 \pm 3.7	52.21	2.14	IRAM 30m	13.8	1, P
$\text{HOC}^+(2 - 1)$	178972.0	823.9 \pm 151.7	1135.3 \pm 16.5	181.1 \pm 38.7	4.27	1.42	IRAM 30m	13.7	1, P

HNC (2 – 1)	181324.7	3678.3 ± 613.2	1115.1 ± 10.1	117.9 ± 20.7	29.30	9.88	IRAM 30m	13.6	1, P
C ³⁴ S (4 – 3)	192818.5	< 920	CSO 10m	...	17
CS (4 – 3)	195954.2	2053 ± 566	CSO 10m	37.1	17
SO (5 ₅ – 4 ₄)	215220.8	553.1 ± 82.9	1135.1 ± 16.7	210.5 ± 34.6	2.47	0.79	IRAM 30m	11.4	2
SiO (5 – 4)	217105.0	479.9 ± 81.1	1117.4 ± 11.1	137.8 ± 27.7	3.27	0.94	IRAM 30m	11.3	2
HC ₃ N (24 – 23)	218324.7	2030 ± 180	1102 ± 13	257.3 ± 24.0	6.2	1.2	SMT 10m	33	18
C ¹⁸ O (2 – 1)	219560.4	3438.3 ± 350.0	1105.4 ± 5.1	173.2 ± 13.8	18.70	1.80	IRAM 30m	11.2	2
		2000 ± 200	1067 ± 12	210 ± 30	9.0	1.9	IRAM 30m	11.2	14
		6842 ± 412	CSO 10m	...	17
SO (5 ₆ – 4 ₅) ^e	219949.4	< 5070.6 ± 364.1	1217.2 ± 20.9	571.6 ± 43.7	8.33	1.80	IRAM 30m	11.2	2
HNCO (10 _{0,10} – 9 _{0,9})	219798.3	< 400 ± 70	...	210	< 2.1	...	IRAM 30m	11.2	14
¹³ CO (2 – 1)	220398.7	13314.0 ± 126.7	1134.8 ± 1.1	224.8 ± 2.3	55.60	1.80	IRAM 30m	11.2	2
		15000 ± 1800	56	...	IRAM 30m	12	15
		17100 ± 2000	46	...	JCMT 15m	21	15
		20790 ± 382	CSO 10m	...	17
CH ₃ CN (12 ₀ – 11 ₀) ^e	220747.3	< 2084.2 ± 385.8	1132.1 ± 36.7	377.9 ± 70.1	5.18	1.80	IRAM 30m	11.1	2
C ¹⁷ O (2 – 1)	224714.4	921 ± 307	CSO 10m	...	17
H ₂ CO (3 _{1,2} – 2 _{1,1})	225697.8	1190.0 ± 170.6	1161.7 ± 14.8	208.3 ± 33.5	5.37	2.13	IRAM 30m	10.9	2
SO ₂ (14 _{3,11} – 14 _{2,12})	226300.0	2947.8 ± 175.5	1097.9 ± 5.8	191.1 ± 12.2	14.49	2.50	IRAM 30m	10.9	2
CN (2 _{3/2,5/2} – 1 _{1/2,3/2})	226659.5	10231.0 ± 372.6	1150.3 ± 3.9	233.1 ± 8.9	41.24	2.50	IRAM 30m	10.9	2
		2808 ± 831	1159 ± 42	265	10.6	3.1	JCMT 15m	21	19
		154	12.2	1.8	SEST 15m	23	12 ^f
CN (2 _{5/2,7/2} – 1 _{3/2,5/2})	226874.8	16479.0 ± 342.2	1144.7 ± 2.3	226.5 ± 4.9	68.36	2.50	IRAM 30m	10.8	2
		8464 ± 672	1151 ± 15	265 ± 35	31.9	2.5	JCMT 15m	21	19
		154 ± 66	20.4	1.8	SEST 15m	23	12 ^f
		14342 ± 265	CSO 10m	...	17
CO (2 – 1)	230538.0	266000 ± 32000	1080	...	IRAM 30m	12	15
		220000 ± 26000	690	...	JCMT 15m	21	15
		203600 ± 20500	1007 ± 2	63 ± 9	313.3	49.2	JCMT 15m	21	12 ^c
		...	1121 ± 4	179 ± 16	802.0	13.3
		...	1245 ± 3	81 ± 10	337.4	57.3
		241711 ± 554	CSO 10m	...	17
CH ₃ CCH (14 _k – 13 _k)	239252.3	1355.4 ± 265.3	1170.5 ± 35.7	344.2 ± 70.4	3.70	1.73	IRAM 30m	10.3	2 ^g
C ³⁴ S (5 – 4)	241016.1	1184 ± 312	CSO 10m	...	17
HNCO (11 _{0,11} – 10 _{0,10})	241774.0	1602.4 ± 194.7	1121.7 ± 14.8	236.4 ± 30.6	6.37	1.66	IRAM 30m	10.2	2
CS (5 – 4)	244935.6	2703.2 ± 187.4	1148.8 ± 6.7	189.8 ± 13.9	13.38	1.88	IRAM 30m	10.0	2
		3300 ± 300	1125 ± 9	180 ± 20	17.6	3	IRAM 30m	10.0	14
		1618 ± 303	CSO 10m	30.8	17
HC ¹⁵ N (3 – 2)	258157.0	< 460(2 σ)	APEX 12m	23.5	5
H ¹³ CN (3 – 2)	259011.8	< 460(2 σ)	APEX 12m	23.5	5
H ¹³ CO ⁺ (3 – 2)	260255.3	< 570(2 σ)	APEX 12m	23.5	5
HN ¹³ C (3 – 2)	261263.4	< 450(2 σ)	APEX 12m	23.5	5
C ₂ H (3 – 2)	262250	1579 ± 259	CSO 10m	...	17
HCN (3 – 2)	265886.2	19000 ± 600	...	220 ± 10	IRAM 30m	9.3	11
		22700 ± 2500	1103 ± 7	275 ± 17	81.2	4.0	JCMT 15m	18	12
		11184 ± 342	CSO 10m	29	17
		4000 ± 600	1145	85	32	7	CSO 10m	27	20
HCO ⁺ (3 – 2)	267557.6	7600 ± 800	...	234 ± 4	IRAM 30m	9.2	11
		7342 ± 461	CSO 10m	29	17
HOC ⁺ (3 – 2)	268451.1	< 526	CSO 10m	...	17
HNC (3 – 2)	271981.1	3500 ± 600	1071 ± 9	134 ± 23	21.5	3.0	JCMT 15m	18	12 ^b
		...	1250 ± 24	70 ± 58	6.2	4.2
		2829 ± 276	CSO 10m	28	17
Unidentified	290020	2500 ± 417	CSO 10m	...	17
CS (6 – 5)	293912.1	1539 ± 513	CSO 10m	26.3	17
CO (3 – 2)	345796.0	166000 ± 20000	630	...	JCMT 15m	14	15
¹³ CO (3 – 2)	330588.0	10700 ± 1300	43	...	JCMT 15m	14	15
CN (3 _{5/2,5/2} – 2 _{5/2,5/2})	339475.9	461 ± 168	1216 ± 33	132	3.5	1.3	JCMT 15m	15	19
CN (3 _{5/2,7/2} – 2 _{5/2,7/2})	339516.7	1048 ± 189	1076 ± 14	132 ± 34	7.9	1.4	JCMT 15m	15	19
CS (7 – 6)	342882.9	1400 ± 500	1125.4 ± 49.0	279.0 ± 99.3	4.8	8.1	JCMT 15m	14	21
HCN (4 – 3)	354505.5	13900 ± 1600	1123 ± 6	202 ± 14	65.9	3.8	JCMT 15m	14	21
		9000 ± 500	JCMT 15m	14	22
HCO ⁺ (4 – 3)	356734.1	3800 ± 500	1112 ± 8	166 ± 19	23.7	2.2	JCMT 15m	14	19
		3400 ± 800	JCMT 15m	14	22

HNC (4 – 3)	362630.3	2700 ± 300	1116 ± 18	218 ± 47	10.6	1.7	JCMT 15m	14	19
CO (4 – 3)	461040.8	290000 ± 35000	1060	...	JCMT 15m	11	15

Notes: The fluxes are in T_{mb} scale. We do not give the uncertainties, which cannot be found in the corresponding literature.

^(a) We fit a Gaussian profile with the velocity and width fixed to the velocity of the HC₃N (10 – 9) transition.

^(b) Two velocity components are included for the Gaussian fitting. The total flux of the CN (1 – 0) transition is 9400 ± 1000 mK km s⁻¹.

^(c) Three velocity components are included for the Gaussian fitting.

^(d) CH₃OH ($J_{1,J-1} - J_{0,J}$)E and SO₂ ($5_{2,4} - 5_{1,5}$) are blended. We fit their profiles with velocities and widths fixed to those of the CH₃OH ($2_k - 1_k$) and SO₂ ($14_{3,11} - 14_{2,12}$) transitions, respectively.

^(e) CH₃CN ($12_0 - 11_0$), ¹³CO (2 – 1), SO ($5_6 - 4_5$) and C¹⁸O (2 – 1) are blended. The integrated intensities of SO ($5_6 - 4_5$) and CH₃CN ($12_0 - 11_0$) are upper limits.

^(f) The total flux of the CN (2 – 1) transition is 6100 ± 700 mK km s⁻¹.

^(g) This transition was newly discovered in the spectra of Qiu et al. (2018).

Reference: (1) this work; (2) Qiu et al. (2018); (3) Takano et al. (2019); (4) Nakajima et al. (2011); (5) Wang et al. (2014); (6) Aladro et al. (2013); (7) Aladro et al. (2015); (8) Nakajima et al. (2018); (9) Costagliola et al. (2011); (10) Usero et al. (2004); (11) Krips et al. (2008); (12) Pérez-Beaupuits et al. (2007); (13) Huettemeister et al. (1995); (14) Martín et al. (2009b); (15) Israel (2009); (16) Mauersberger et al. (1989); (17) Kamenetzky et al. (2011); (18) Jiang et al. (2017); (19) Pérez-Beaupuits et al. (2009); (20) Paglione et al. (1997); (21) Bayet et al. (2009); (22) Tan et al. (2018).

Remarks: (P) measurements based on the present observations; (A) measurements based on the co-added spectra of the present observations and those of Qiu et al. (2018) and Aladro et al. (2013); (C) measurements based on the coadded spectra of our observations and those of Qiu et al. (2018).

Table 3. Flux ratios (row/column).

	$^{13}\text{CCH} (2-1)$	$\text{HCN} (2-1)$	$\text{HCO}^+ (2-1)$	$\text{HOC}^+ (2-1)$	$\text{HNC} (2-1)$
$^{13}\text{CCH} (2-1)$	1.00 ± 0.28	0.013 ± 0.003	0.024 ± 0.005	0.38 ± 0.10	0.085 ± 0.022
$\text{HCN} (2-1)$	75.3 ± 15.1	1.00 ± 0.01	1.82 ± 0.03	28.7 ± 5.28	6.42 ± 1.07
$\text{HCO}^+ (2-1)$	41.4 ± 8.34	0.55 ± 0.008	1.00 ± 0.02	15.8 ± 2.91	3.53 ± 0.59
$\text{HOC}^+ (2-1)$	2.63 ± 0.72	0.035 ± 0.006	0.063 ± 0.012	1.00 ± 0.26	0.22 ± 0.056
$\text{HNC} (2-1)$	11.7 ± 3.07	0.16 ± 0.03	0.28 ± 0.047	4.46 ± 1.11	1.00 ± 0.24

Table 4. Flux ratios of the blue and red components of the CDN lines.

Transition	Flux(blue) mK km s ⁻¹	Flux(red) mK km s ⁻¹	R _{E/w}
$\text{HC}_3\text{N} (18-17)$	405	175	2.32 ± 0.28
$\text{SiO} (5-4)$	281	135	2.08 ± 0.57
$\text{SO}_2 (14_{3,11} - 14_{2,12})$	2123	1034	2.05 ± 0.16
$\text{HNC} (2-1)$	1994	1175	1.70 ± 0.46
$\text{HCN} (2-1)$	13376	9116	1.47 ± 0.02
$\text{HCO}^+ (2-1)$	7203	5231	1.38 ± 0.03
$\text{HNCO} (11-10)$	918	701	1.31 ± 0.22
$^{13}\text{CCH} (2-1)$	148	114	1.30 ± 0.49
$\text{CH}_3\text{CN} (9-8)$	160	140	1.14 ± 0.34
$\text{SO} (5_5 - 4_4)$	259	279	0.93 ± 0.20
$\text{HOC}^+ (2-1)$	402	432	0.93 ± 0.24
$\text{CS} (5-4)$	1154	1462	0.79 ± 0.08
$\text{CH}_3\text{CCH} (14_k - 13_k)$	403	592	0.68 ± 0.26
$\text{H}_2\text{CO} (3_{1,2} - 2_{1,1})$	436	649	0.67 ± 0.15

Notes. Columns 2 and 3 list the fluxes of the blue and red components, respectively. Column 4 shows the flux ratios of the blue-to-red (east-to-west) components.

Table 5. Rotational temperatures and column densities of the observed molecules.

Molecule	lines	T_{rot} K	N_{mol} cm^{-2}	Telescope	Ref
CS	(2-1) (3-2) (5-4)	6.60 ± 0.12	$(8.78 \pm 0.47) \times 10^{14} \text{ cm}^{-2}$	IRAM 30m	1, 5, 2
	(5-4)(7-6)	41.56 ± 17.82	$(6.01 \pm 2.31) \times 10^{13} \text{ cm}^{-2}$	IRAM, JCMT	2, 6
HC ₃ N	(9-8)(10-9)(11-10)(12-11)(18-17)	17.75 ± 0.60	$(1.59 \pm 0.10) \times 10^{14} \text{ cm}^{-2}$	IRAM 30m	1, 2, 7, 7,1
HCN	(1-0)(2-1)(3-2)(3-2)(4-3)	17.32 ± 0.49	$(6.78 \pm 0.15) \times 10^{13} \text{ cm}^{-2}$	IRAM, JCMT	2, 1, 8, 9, 4
HCO ⁺	(1-0)(2-1)	3.03 ± 0.02	$(5.81 \pm 0.05) \times 10^{14} \text{ cm}^{-2}$	IRAM 30m	2, 1
	(3-2)(4-3)	27.02 ± 9.95	$(2.33 \pm 0.94) \times 10^{13} \text{ cm}^{-2}$	IRAM, JCMT	8, 10
HNC	(1-0)(2-1)	2.51 ± 0.11	$(5.24 \pm 0.41) \times 10^{14} \text{ cm}^{-2}$	IRAM 30m	2, 1
	(3-2)(4-3)	13.31 ± 1.93	$(7.98 \pm 3.40) \times 10^{13} \text{ cm}^{-2}$	JCMT 15m	9, 4
HOC ⁺	(1-0)(2-1)	5.68 ± 0.78	$(1.82 \pm 0.36) \times 10^{13} \text{ cm}^{-2}$	IRAM 30m	2, 1
SiO	(2-1)(3-2)	3.16 ± 0.19	$(1.03 \pm 0.18) \times 10^{14} \text{ cm}^{-2}$	IRAM 30m	2, 11
	(3-2)(5-4)	8.55 ± 0.71	$(2.30 \pm 0.44) \times 10^{13} \text{ cm}^{-2}$	IRAM 30m	11, 2
CH ₃ CN	(5-4)(6-5)(9-8)	7.88 ± 0.51	$(8.90 \pm 1.65) \times 10^{13} \text{ cm}^{-2}$	IRAM 30m	1, 7,1
SO	(2-1)(3-2)(5-4)	14.13 ± 1.46	$(2.14 \pm 0.58) \times 10^{14} \text{ cm}^{-2}$	IRAM 30m	3, 3, 2
HNCO	(4-3)(5-4)(11-10)	19.77 ± 0.85	$(5.70 \pm 0.39) \times 10^{14} \text{ cm}^{-2}$	IRAM 30m	2, 12, 2
CN	(1-0) (2-1)	5.63 ± 0.38	$(1.38 \pm 0.27) \times 10^{15} \text{ cm}^{-2}$	IRAM 30m	3, 2
	(2-1) (3-2)	62.50 ± 89.87	$(9.78 \pm 5.08) \times 10^{14} \text{ cm}^{-2}$	JCMT 15m	4, 4
CH ₃ OH ^a	(2-1)(J-J)	6.70 ± 0.48	$(2.34 \pm 0.52) \times 10^{15} \text{ cm}^{-2}$	IRAM 30m	1, 1
	(J-J)(5-4)	50.09 ± 32.01	$(3.90 \pm 1.32) \times 10^{15} \text{ cm}^{-2}$	IRAM 30m	1, 2
SO ₂	(14-14)(5-5)	4.61 ± 0.39	$(6.29 \pm 1.21) \times 10^{14} \text{ cm}^{-2}$	IRAM 30m	2,1
CH ₃ CCH	(5-4)(14-13)	28.01 ± 3.43	$(3.30 \pm 1.04) \times 10^{15} \text{ cm}^{-2}$	IRAM 30m	2,1
CH ₃ OCH ₃	(3 _{2,2} -3 _{1,3})	10^b	$(3.16 \pm 1.01) \times 10^{15} \text{ cm}^{-2}$	IRAM 30m	1
N ₂ H ⁺	(1-0)	10^b	$(7.63 \pm 1.24) \times 10^{13} \text{ cm}^{-2}$	IRAM 30m	1
¹³ CCH	(2-1)	10^b	$(3.35 \pm 0.78) \times 10^{14} \text{ cm}^{-2}$	IRAM 30m	1

Notes. ^(a) Owing to the emission of CH₃OH ($5_{-1,5} - 4_{0,4}$)E comes from a mega-maser (Wang et al. 2014), the rotation temperature of its warmer component is an upper limit. ^(b) The rotation temperature is assumed to be 10 K.

Reference: (1) this work; (2) Qiu et al. (2018); (3) Aladro et al. (2013); (4) Pérez-Beaupuits et al. (2009); (5) Mauersberger et al. (1989); (6) Bayet et al. (2009); (7) Aladro et al. (2015); (8) Krips et al. (2008); (9) Pérez-Beaupuits et al. (2007); (10) Tan et al. (2018); (11) Usero et al. (2004); (12) Martín et al. (2009b).

Table 6. Integrated intensity ratios shown in Fig. 7.

Transition	Frequency GHz	I_1 mK km s ⁻¹	I_2 mK km s ⁻¹	R	θ_{b1} "	θ_{b2} "	θ_s "	Ref(1)	Ref(2)	Marks
¹³ CO(1-0)	110.2	8900 ± 200	13100 ± 240	0.68 ± 0.02	16.5	22.3	...	3	5	NRO45m / IRAM30m
CH ₃ OH(2 _k - 1 _k)	96.7	1100 ± 200	1613 ± 271	0.68 ± 0.17	19.0	25.4	...	3	1	NRO45m / IRAM30m
HNC(1-0)	90.7	5600 ± 400	7836 ± 35	0.71 ± 0.05	19.1	27.1	...	3	2	NRO45m / IRAM30m
¹³ CO(2-1)	220.4	13314 ± 127	17100 ± 2000	0.78 ± 0.09	11.2	21.0	...	2	8	IRAM30m / JCMT15m
HCN(3-2)	265.9	19000 ± 600	22700 ± 2500	0.84 ± 0.10	9.8	18.0	...	7	10	IRAM30m / JCMT15m
C ¹⁸ O(1-0)	109.8	3300 ± 200	3900 ± 90	0.85 ± 0.05	16.5	22.4	...	3	5	NRO45m / IRAM30m
CO(1-0)	115.3	155000 ± 1000	172200 ± 4500	0.90 ± 0.02	15.2	21.3	...	3	4	NRO45m / IRAM30m
SiO(2-1)	86.8	800 ± 200	879 ± 65	0.91 ± 0.24	18.7	28.3	...	3	2	NRO45m / IRAM30m
HCO ⁺ (1-0)	89.2	13300 ± 700	14519 ± 56	0.92 ± 0.05	19.1	27.6	...	3	2	NRO45m / IRAM30m
CS(2-1)	98.0	5400 ± 200	5701 ± 239	0.95 ± 0.05	19.0	25.1	...	3	1	NRO45m / IRAM30m
c-C ₃ H ₂ (21 ₂ - 10 ₁)	85.3	1200 ± 100	1190 ± 60	1.01 ± 0.10	19.0	28.8	239 ± 1448	3	2	NRO45m / IRAM30m
CN(1 _{3/2,5/2} - 0 _{1/2,3/2})	113.5	27600 ± 400	25790 ± 190	1.07 ± 0.02	15.2	21.7	56 ± 8	3	5	NRO45m / IRAM30m
H ¹³ CN(1-0)	86.3	1400 ± 200	1250 ± 37	1.12 ± 0.16	18.7	28.5	59 ± 44	3	2	NRO45m / IRAM30m
CO(2-1)	230.5	266000 ± 32000	220000 ± 26000	1.21 ± 0.20	10.6	21.0	38 ± 20	8	8	IRAM30m / JCMT15m
C ₂ H(1-0)	87.3	10000 ± 300	7940 ± 53	1.26 ± 0.04	19.0	28.2	36 ± 3	3	2	NRO45m / IRAM30m
HCN(1-0)	88.6	26400 ± 600	20754 ± 29	1.27 ± 0.03	19.1	28.0	34 ± 2	3	2	NRO45m / IRAM30m
CN(1 _{1/2,3/2} - 0 _{1/2,3/2})	113.2	18500 ± 300	13150 ± 100	1.41 ± 0.03	15.2	21.7	19 ± 1	3	5	NRO45m / IRAM30m
CH ₃ CN(6 _k - 5 _k)	110.4	1000 ± 200	700 ± 490	1.43 ± 1.04	16.5	22.3	16 ± 40	3	5	NRO45m / IRAM30m
N ₂ H ⁺ (1-0)	93.2	2100 ± 400	1407 ± 229	1.49 ± 0.37	19.1	26.4	18 ± 15	3	1	NRO45m / IRAM30m
HC ₃ N(12-11)	109.2	1300 ± 100	850 ± 40	1.53 ± 0.14	16.5	22.5	13 ± 4	3	5	NRO45m / IRAM30m
SO(2 ₃ - 1 ₂)	99.3	800 ± 200	470 ± 60	1.70 ± 0.48	16.5	24.8	15 ± 11	3	5	NRO45m / IRAM30m
CN(2 _{5/2,7/2} - 1 _{3/2,5/2})	226.9	16479 ± 342	8464 ± 672	1.95 ± 0.16	10.9	21.0	15 ± 2	2	9	IRAM30m / JCMT15m
¹³ CN(1 _{1/2} - 0 _{1/2})	108.7	400 ± 100	200 ± 100	2.00 ± 1.12	16.5	22.5	...	3	4	NRO45m / IRAM30m
HC ₃ N(11-10)	100.1	1600 ± 300	800 ± 40	2.00 ± 0.34	16.5	24.6	8 ± 8	3	5	NRO45m / IRAM30m
HNCO(4 _{0,4} - 3 _{0,3})	87.9	1600 ± 200	675 ± 45	2.37 ± 0.34	19.1	28.0	...	3	2	NRO45m / IRAM30m
HNCO(5 _{0,5} - 4 _{0,4})	109.9	900 ± 100	300 ± 150	3.00 ± 1.54	16.5	22.4	...	3	4	NRO45m / IRAM30m
CN(2 _{5/2,7/2} - 1 _{3/2,5/2})	226.7	10231 ± 373	2808 ± 831	3.64 ± 1.09	10.9	21.0	2 ± 14	2	9	IRAM30m / JCMT15m
HC ₃ N(10-9)	91.0	4700 ± 1000	929 ± 36	5.06 ± 1.09	19.1	27.0	...	3	1	NRO45m / IRAM30m
H ¹³ CO ⁺ (1-0)	86.8	< 150	758 ± 39	< 0.20	18.7	28.4	...	3	2	NRO45m / IRAM30m
CH ₃ CCH(5 _k - 4 _k)	85.5	< 140	348 ± 107	< 0.40	19.0	28.8	...	3	2	NRO45m / IRAM30m
SO(3 ₂ - 2 ₁)	109.3	< 250	200 ± 100	< 1.25	16.5	22.5	< 26	6	4	NRO45m / IRAM30m
SO(5 ₄ - 4 ₄)	100.0	< 500	200 ± 100	< 2.00	16.5	24.6	...	6	4	NRO45m / IRAM30m

Notes. Columns 1 and 2 list the transitions and frequencies, respectively. Columns 3 and 4 list the detected integrated intensities with the NRO 45m (or IRAM 30m) and IRAM 30m (or JCMT 15m) telescopes, respectively. Column 5 lists the ratios between the intensities given in Cols. 3 and 4. Columns 6 and 7 list the beam sizes of the NRO 45m (or IRAM 30m) and the IRAM 30m (or JCMT 15m) telescopes, respectively. Column 8 lists the estimated source sizes. Columns 9 and 10 list the references for the data listed in Cols. 1 and 2, respectively.

Reference: (1) this work; (2) Qiu et al. (2018); (3) Takano et al. (2019); (4) Aladro et al. (2013); (5) Aladro et al. (2015);

(6) Nakajima et al. (2018); (7) Krips et al. (2008); (8) Israel (2009); (9) Pérez-Beaupuits et al. (2009); (10) Pérez-Beaupuits et al. (2007).